SOIL CO_2 FLUX AND TEMPERATURE FROM A NEW GEOTHERMAL AREA IN THE CORDÓN DE INACALIRI VOLCANIC COMPLEX (NORTHERN CHILE)

Taussi Marco [a]*, Nisi Barbara [b], Vaselli Orlando [b,c,d], Maza Santiago[e,f], Morata Diego [e,f], Renzulli Alberto [a,g]

[a] *Dipartimento di Scienze Pure e Applicate, Università degli Studi di Urbino Carlo Bo, Via Ca' Le Suore 2/4, Urbino, Italy*

[b] *CNR-IGG Istituto di Geoscienze e Georisorse, Consiglio Nazionale delle Ricerche, Via G. La Pira 4, Florence, Italy*

[c] *Dipartimento di Scienze della Terra, Università di Firenze, Via G. La Pira 4, Florence, Italy*

[d] *INGV-Bologna, Via Franceschini 31, Bologna, Italy*

[e] *Departamento de Geología, Facultad de Ciencias Físicas y Matemáticas, Universidad de Chile, Plaza Ercilla 803, Santiago, Chile*

[f] *Centro de Excelencia en Geotermia de los Andes (CEGA), Universidad de Chile, Plaza Ercilla 803, Santiago, Chile*

[g] *Geo.In.Tech. srl Spin Off, Università degli Studi di Urbino Carlo Bo, Via Ca' Le Suore 2/4, Urbino, Italy*

***** Corresponding author: e-mail address: marco.taussi@uniurb.it (M. Taussi).

Keywords: Geothermal exploration - CO_2 diffuse degassing - Heat flux - High-altitude geothermal system - Thermal energy - Andean Cordillera - Chile

Abstract

This paper deals with the first geochemical data from an unexplored sector of the Cordón de Inacaliri Volcanic Complex (Central Andes, Chile). The site is located at ~5,150-5,200 m a.s.l., inside the Pabelloncito graben where, at about 9 km NW of the studied area, the only currently working geothermal power plant of South America, named Cerro Pabellón, occurs. Diffuse soil CO_2 and soil temperature measurements were carried out to unravel the structural control on the rising fluids and estimate the total CO_2 output, the heat flow rate and the heat flux, aimed at assessing a preliminary evaluation of the geothermal potential of the area. The study area is characterized by a pervasive hydrothermal mineralogical alteration, CO_2 flux values of up to ~4,400 g m^{-2} d^{-1} and soil temperatures up to the boiling point of water at that altitude. All these features are likely related to an endogenous source. Spatial distribution of both soil CO_2 flux and temperature depict an ENE-striking lineament, whose intersection with the NW-striking Pabelloncito graben forms a favourable structural setting for the discharge of hydrothermal fluids. The total CO_2 output emission of the studied area (~0.0179

km^2) was ~0.53 t d^{-1}, with an associated discharge of steam of 6.45 t d^{-1} (CO_2/H_2O ratio = 0.08). An electric capacity potential of 1.08 MWe km^{-2} was computed from the heat flow rate and heat flux values. Our results suggest that this part of the Pabelloncito graben is an interesting geothermal prospect and a good candidate for further exploration studies.

1. Introduction

Geothermal (high temperature) anomalies in South America are mainly located along the Andean Cordillera in close spatial relationships with active volcanism, which is primarily controlled by the convergence of the Nazca and South American Plates (Lahsen et al., 2015; Aravena et al., 2016). The great potential in terms of renewable energy production is testified by both recent discoveries and assessments of geothermal areas along the Andes (e.g. Procesi, 2014; Aravena et al., 2016; Chiodi et al., 2019; Barcelona et al., 2019; Gómez Diaz and Marín Cerón, 2020) and new geothermal exploitation and exploration projects developed in Chile (e.g. Apacheta-Cerro Pabellón, El Tatio, La Torta, Olca; Mesa de Geotermia, 2018; Morata et al., 2020a) and Bolivia (e.g. Laguna Colorada and Salar de Empexa; Villarroel, 2020) (Fig. 1). It was estimated that the geothermal power potential of Chile is approximately of 2,000 MWe, representing one of the most attractive countries in the World for the installations of future geothermal plants (e.g. Procesi et al., 2014; Aravena et al., 2016). The main Chilean geothermal systems are mostly located in the northern (17-28 °S) and central-southern (33-46 °S) sectors of the country (Lahsen et al., 2015), the former consisting of about 90 identified thermal emission areas (Hauser, 1997), although by March 2018, only 5 out of 9 exploration licenses were active and 4 are the areas presently in force (Mesa de Geotermia, 2018). Unfortunately, the low population density in the Cordillera, the remoteness of most hydrothermal systems and the political-economic difficulties (i.e. financial, economic, institutional and legal/regulatory barriers; Sanchéz-Alfaro et al., 2015) are slowing down the exploitation of the geothermal resources in Chile. As a matter of fact, Cerro Pabellón (Chile), a blind (or hidden) geothermal system, whose only surface hydrothermal manifestation is represented by the fumarolic field located on the top of the nearby Apacheta-Aguilucho Volcanic Complex (Maza et al., 2018a; Taussi et al., 2019a), is the only active geothermal power plant in South America, with a power capacity of 48 MWe (already installed) and an additional 33 MWe unit which is presently under-construction (enelgreenpower.com).

Despite the large amount of geothermal systems along and across the Central Andes, where geysers, fumaroles, cold and hot mud pools and thermal water discharges were recognized (e.g. Hauser, 1997; Tassi et al., 2010; Risacher et al., 2011; Lahsen et al. 2015; Sanchez-Alfaro et al. 2015; Veloso et al., 2019), there are still completely unexplored hydrothermal areas such as that belonging to the Cordón de Inacaliri Volcanic Complex. This volcanic complex is Pleistocene in age (Sellés and Gardeweg, 2017) and is located in the south-easternmost part of the Pabelloncito graben, at about 9 km from the Apacheta-Aguilucho Volcanic Complex and the Pampa Apacheta, where the Cerro Pabellón geothermal power plant is in operation since 2017. The Cordón de Inacaliri area is characterized by an extensive hydrothermal alteration and steaming grounds, and in the past, it was even exploited for mineral ore deposits (mainly sulphur; Sellés and Gardeweg, 2017).

Since CO_2 is one of the most abundant gases in volcanic-geothermal systems, a diffuse soil CO_2 flux survey coupled with soil temperature measurements, was carried out (from 7 to 9 December 2017) in order to provide the very first characterization of heat and CO_2 flux of this unexplored hydrothermal system in the Chilean Andes. Diffuse soil CO_2 flux measurement is a useful technique widely used for i) mapping sub-surface volcano-tectonic structures (e.g. Giammanco et al., 2016), ii) quantifying heat and mass flow (e.g. Bloomberg et al., 2014; Chiodini et al., 2015), iii) monitoring active volcanoes (e.g. Cardellini et al., 2017), iv) determining the sealing capacity of the cap-rock (or clay-cap units) of geothermal reservoirs (Carapezza et al., 2015; Taussi et al., 2019a) and v) assessing the geogenic CO_2 emitted from volcanic areas (e.g. Fischer and Aiuppa, 2020).

The proximity to the Cerro Pabellón geothermal power plant, the presence of relatively extensive acid-sulphate hydrothermal alteration areas and steaming grounds related to a recent circulation of hot hydrothermal fluids and the occurrence of an extensional tectonic structure (i.e. the Pabelloncito graben), likely acting as a preferential pathway for the CO_2 degassing (e.g. Tamburello et al., 2018; Lamberti et al., 2019), suggests the need to undertake an evaluation of the local geothermal potential at Cordón de Inacaliri. Consequently, this paper is aimed to evaluate: i) the total CO_2 output ii) the heat flux of the Cordón de Inacaliri hydrothermal system and iii) the structural control on the fluid circulation, in order to give a preliminary assessment of the geothermal potential of this unexplored area.

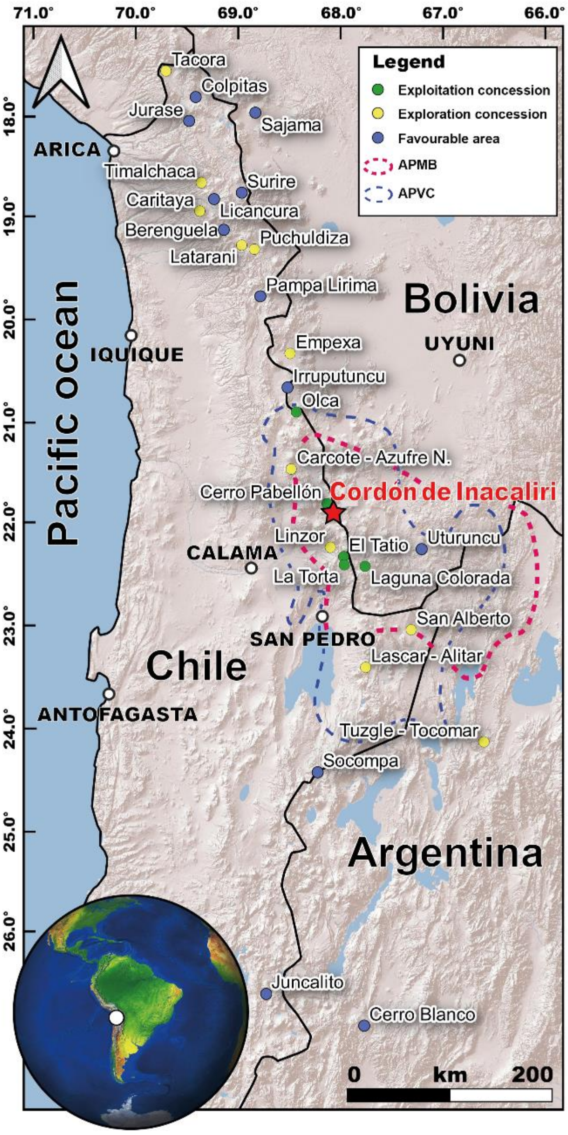

Fig. 1 - General view of the Central Andes and location of the study area in the framework of the main geothermal sites of Chile, Bolivia and Argentina, distinguished by exploration (active and not active) and exploitation concessions and favourable areas (after Giordano et al., 2013; Lahsen et al., 2015; Aravena et al., 2016; Bona and Coviello, 2016; Lelli, 2018; Mesa de Geotermia, 2018; Chiodi et al., 2019; Veloso et al., 2019; Morata et al., 2020a). The surface projection of the Altiplano-Puna Volcanic Complex (APVC) and the Altiplano-Puna Magma Body (APMB) are also reported (after de Silva, 1989 and Ward et al., 2014).

2. Geological background

The study area is part of the Pleistocene Cordón de Inacaliri Volcanic Complex (CIVC; Sellés and Gardeweg, 2017). The CIVC is about 15 km long, extending from the Pampa Apacheta to NW, to the Bolivian territory to the S. It hosts three main stratovolcanoes whose eruptive centres are approximately NW-SE aligned (Fig. 2), being distributed according to the main local tectonic fault systems (Tibaldi et al., 2010). An additional eruptive centre, the Inacaliri Volcano (5,618 m a.s.l.), is located about 6 km to S from the studied area (Fig. 3).

All the CIVC volcanic products are partially interlayered and erupted by the three summit craters, suggesting stable central conduits and a general coeval growth of the volcanic complex (Tibaldi et al., 2010). This is apparently confirmed by new $^{40}Ar/^{39}Ar$ age dating (Sellés and Gardeweg, 2017), constraining the CIVC activity between ~1.6 and ~1.0 Ma. The volcanic complex is constituted by andesitic to rhyolitic lava flows (56.8-69.9% SiO_2; Piscaglia, 2011; Sellés and Gardeweg, 2017), while the Inacaliri volcano is mainly andesitic (González-Ferrán, 1995). Both CIVC and Inacaliri volcano lie above the Miocene Sifón ignimbrite (de Silva, 1989; Sellés and Gardeweg, 2017), which is part of the Altiplano-Puna Volcanic Complex (APVC), an ignimbritic plateau located between 21° and 24°S and straddling Chile, Bolivia and Argentina (Fig. 1). The overthickened crust of APVC (up to 70 km; Beck et al., 1996) hosts, at about 10-20 km of depth, a partially-molten amalgamated igneous body called Altiplano-Puna Magma Body (Fig. 1; APMB; Ward et al., 2014 and references therein), which is thought to be the source of a large-scale silicic magmatism since ca. 10 Ma, during which a cumulative volume of >10,000 km^3 of ignimbrites was erupted (Salisbury et al. 2011).

The CIVC is located inside the Pabelloncito graben (Francis and Rundle, 1976) that is characterized by two major NW-striking tectono-morphological lineaments, sometimes dislocated by NE-striking faults (Fig. 2), with converging dip angles and opposite-facing scarps. Consequently, a ~4 km wide and ~20 km long structure that runs from the Apacheta-Aguilucho Volcanic Complex (AAVC) and Cerro del Azufre to the Inacaliri volcano is depicted (Fig. 3). In the NW end of the southern fault of the Pabelloncito graben, the AAVC (≥1 to ca. 0.6 Ma; Fig.2) is located, with an activity reflecting a transition from high-flux (i.e. flare-ups) to steady state magmatism in the APVC (Taussi et al., 2019b; Godoy et al., 2019).

Additional NW-striking minor normal faults, each from 2 to 4 km long (Tibaldi and Bonali, 2018), affect the Pabelloncito graben (Fig. 2). These faults offset a series of NW-SE-aligned Pleistocene-aged volcanic structures (Sellés and Gardeweg, 2017) and lava flows dated 0.91 ± 0.14 Ma (Rivera et al., 2015). After the end of the volcanic activity of the AAVC, the substratum faults propagated across the entire complex in the late Quaternary, and a new volcanic phase resumed with the emplacement of the Pabellón lava dome (80.0–130.0 ka according to Renzulli et al., 2006 and 50.0 ± 10.0 ka according to Urzua et al., 2002) along the main northern fault bounding the graben.

The Pabelloncito graben formed during a Late Pliocene-Quaternary extensional phase (Tibaldi et al., 2009) and is linked to gravity spreading of the volcanic chain (Tibaldi and Bonali, 2018). It corresponds to an Andean Transverse Fault, consisting of faults and lineaments that obliquely crosscut the Andean belt and represent the main pathways for fluid migration towards shallower crustal levels (Veloso et al., 2019). It is worth to mention that surface geothermal manifestations, stratovolcanoes, monogenetic cones and hydrothermal systems from the Central Andes are commonly developed along either NW-striking faults or splayed off E-striking faults (e.g. Giordano et al., 2013; Godoy et al., 2014; Rivera et al., 2015; Tibaldi and Bonali, 2018; Veloso et al., 2019).

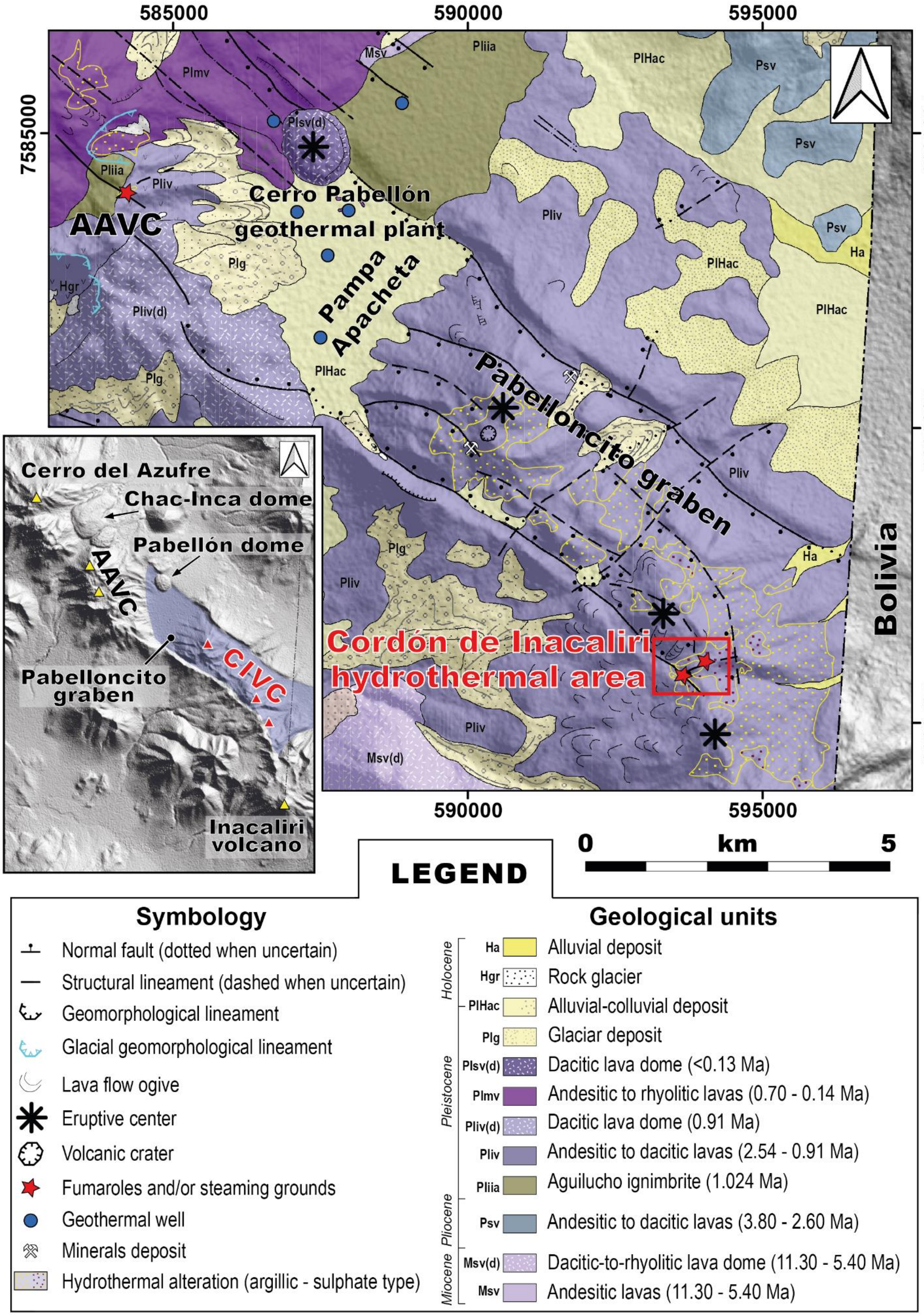

Fig. 2 - Geological map of the Pabelloncito graben with the main tectonic structures (modified from Sellés and Gardeweg, 2017). Known (after Urzua et al., 2002 and Tassi et al., 2010) and new (this

study) surface thermal manifestations from AAVC and CIVC are also reported. Descriptions and acronyms of the geological units are listed according to Sellés and Gardeweg (2017). The inset figure shows the main volcanological features of the area and the approximate extension of the Pabelloncito graben (pale blue). CIVC: Cordón de Inacaliri Volcanic Complex; AAVC: Apacheta-Aguilucho Volcanic Complex. Studied area is marked with the red square. Reference system: WGS84-UTM zone 19S.

3. Field description

The Cordón de Inacaliri study area is located at an altitude of about 5,150 m a.s.l. in the Antofagasta region (northern Chile), 9 km SE of the Cerro Pabellón geothermal system, 45 km N from El Tatio and about 60 km NNW from the La Torta and the Laguna Colorada geothermal prospects (Fig. 1). The investigated area lies within the southern part of the Pabelloncito graben (Fig. 2) where extensive whitish-yellowish-reddish hydrothermal alteration fields occur (Figs. 2 and 3).

The surface manifestations are mostly represented by steaming grounds and hydrothermal incipient fumarole vents located in both the Western (Cordón de Inacaliri Western Sector - CIWS; Fig. 3d,e) and Eastern (Cordón de Inacaliri Eastern Sector - CIES; Fig. 3b,c) sectors (Fig. 3). The area is mainly flat with a hill dividing the two investigated sectors (CIWS and CIES; Fig. 3a). This hill is a small, elliptical (about 300*200 m) and ENE-WSW oriented structure, which rise about 50-100 m high above the ground (maximum elevation 5,250 m a.s.l.) and is characterized by a rough dome-like morphology with steep flanks. A clay-rich homogeneous-distributed soil is present throughout the investigated area where the vegetation, when present, mainly consists of small scattered shrubs (Fig. 3d). From CIES toward the central part of the graben, a marked ENE-striking ridge stretches for about 600 m (Fig. 3a,f) at the end of which the relic of an ancient fumarolic chimney was found (Fig. 3f).

The hydrothermal alteration of the CIVC area is poorly studied and roughly associated with an argillic alteration (Hubbard and Crowley, 2005; Sellés and Gardeweg, 2017; Morata et al., 2020b). Preliminary results highlighted the presence of a mineral zonation characterized by alunite ± cristobalite ± kaolinite with minor amounts of gypsum, halloysite and tridymite in the central areas (i.e. where the steaming grounds occur) and a smectite ± illite-smectite assemblage in the peripheral zone (Maza et al., 2020). Around the small fumarolic orifices, cristobalite ± alunogen ± native sulphur and subordinate kaolinite, quartz, alunite, and hematite were recognized (Maza et al., 2020).

Fig. 3 - a) Satellite view of the Southern area of the Pabelloncito graben where the studied sites of Cordón de Inacaliri Eastern Sector (CIES) and Cordón de Inacaliri Western Sector (CIWS) are indicated along with the dome-like morphological structure (DLS) and the ENE-striking ridge. Field photographs of the Cordón de Inacaliri hydrothermal area refer to b-c) CIES thermal features; d-e) scarceness of vegetation, mineralogical alteration and rough morphology of the DLS at CIWS and f) view of the ENE-striking ridge from CIES toward NE (the inset photo shows the relics of an ancient fumarolic chimney at the end of the ridge). The main fluid vents are indicated with the yellow arrows. AAVC: Apacheta-Aguilucho Volcanic Complex.

4. Methodology

In the first half of December 2017 (with dry and stable atmospheric conditions), 216 and 97 diffuse CO_2 flux measurements were performed at CIWS and CIES, respectively. Soil CO_2 flux measurements were carried out following the accumulation chamber method (e.g. Chiodini et al., 1998). As reported by the manufacturing company (https://www.westsystems.eu/it), the instrumental detection limit is ~0.08 g·m^{-2}·day^{-1}. The instrument was calibrated at the manufacturing company (West Systems) before the survey. The equipment consisted of a cylindrical metal vessel (the accumulation chamber), an Infra-Red spectrophotometer, an analog-digital converter, and a palmtop computer. The accumulation chamber had a volume of ~2.8 L and equipped with a ring-shaped perforated manifold to re-inject the circulating gas through a low-flux pump (20 mL s^{-1}) thus, ensuring the mixing of the soil gas into the chamber. The Infra-Red spectrometer was a LICOR Li-820 detector equipped with a sensor operating in the range 0-20,000 ppm of CO_2. The soil gas circulated from the chamber to the Infra-Red sensor and vice versa by a pump (~1 L min^{-1}). The signal was converted by the analog-digital converter and transmitted to the palmtop computer, where a CO_2 concentration vs. time diagram was plotted in real time. Soil temperature was measured at each site, within 0.01 m from the accumulation chamber, using a Hanna HI-935005N K-Thermocouple (accuracy of ± 0.1 °C) in the first 10 cm. The investigated areas were covered as much as possible with a regular grid, whose nods were located with a portable GPS Garmin Etrex 10, at a 5-10 m grid spacing. The spatial distribution of the diffuse CO_2 soil gas and temperature spots, as well as their density were partly influenced by uneven and/or soft grounds and by the presence of compact hard lavas that cropped out in several zones. CIWS and CIES extend for 0.0145 km^2 and 0.0034 km^2, respectively. Ambient air temperature and barometric pressure were recorded for each sample site, to control possible changes in atmospheric conditions that could exert a significant influence on soil flux measurements (e.g. Lelli and Raco, 2017).

All the data are reported in the Supplementary Material S1 and were analyzed by using the Graphical Statistical Analysis (GSA) method (Chiodini et al., 1998), performed according to the procedure proposed by Sinclair (1974). The distribution map of the soil CO_2 flux and temperature were constructed using the log-normal Kriging method (e.g., Krige 1951; Matheron 1970) by means of Isatis© software package of Geovariances. The maps were then graphically reported using the QGIS software.

5. Results

5.1 Cordón de Inacaliri Western Sector (CIWS)

The soil CO_2 flux values at CIWS ranged from 0.18 g·m^{-2}·day^{-1} to 790.66 g·m^{-2}·day^{-1} with an arithmetic and a geometric mean of 24.42 and 6.53 g·m^{-2}·day^{-1}, respectively. The median value was 8.16 g·m^{-2}·day^{-1} while the standard deviation was ± 75.52 g·m^{-2}·day^{-1}. Soil temperatures were ranging between 1.6 and 80.3 °C, with an arithmetic and a geometric mean of 23.78 and 20.98 °C, respectively. The median value and the standard deviation were 23.10 °C and ± 11.43 °C, respectively.

The cumulative frequency plot of the ln-soil CO_2 efflux data does not show any clear inflection point, suggesting the presence of a single population (Fig. 4a). Setting aside the two outliers (i.e. values of

CO_2 flux higher than 670 g·m^{-2}·day^{-1}), highlighted by the boxplot and the lowest values (i.e. <0.27 g·m^{-2}·day^{-1}) and likely influenced by the proximity to the instrumental detection limit, making the shape of the curve at these low levels uncertain, the dataset shows a (log)normal distribution, confirmed by the histogram in Fig. 4a. The lowest values only represented the 3% of the CIWS dataset, which makes their contribution practically negligible.

The histogram of the soil temperatures (Fig. 4b) apparently show a normal distribution, but an inflection point in the cumulative frequency plot at the 93.1th percentile (i.e. 38.3 °C) can be observed, thus suggesting the presence of at least two populations. From the boxplot, 7 outliers can be identified, which represent values higher than ~45 °C. The main statistical parameters of the two soil temperatures populations of the CIWS are synthetized in Table 1.

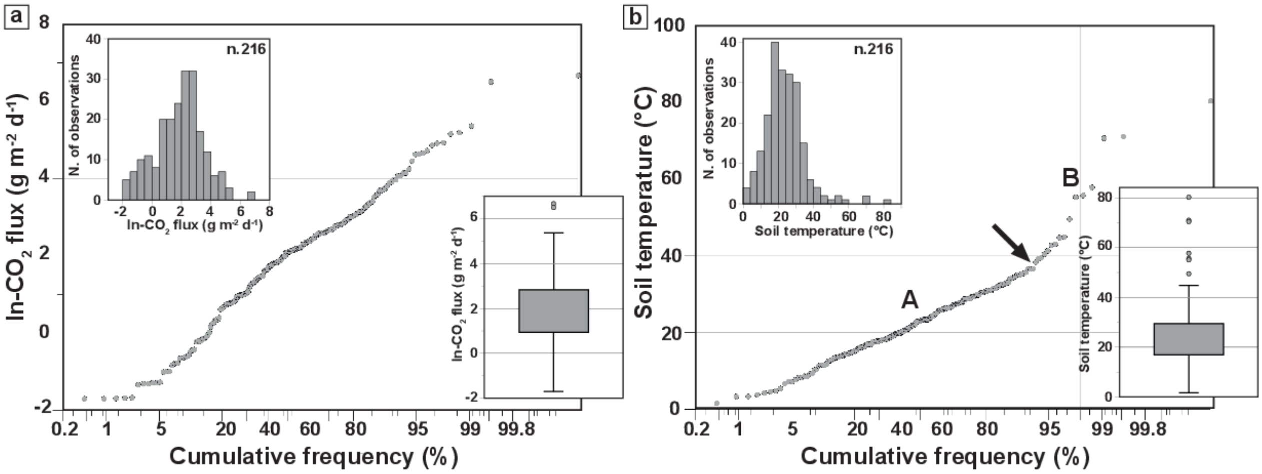

Fig. 4 - Cumulative frequency plots, histograms and boxplots of the (a) soil CO_2 and (b) temperature measurements in the Cordón de Inacaliri Western Sector (CIWS).

5.2 Cordón de Inacaliri Eastern Sector (CIES)

Soil CO_2 flux values at CIES were varying from 0.09 g·m^{-2}·day^{-1} (i.e. close to the lower instrumental detection limit) to 4,425.10 g·m^{-2}·day^{-1} with an arithmetic and a geometric mean of 62.14 and 4.48 g·m^{-2}·day^{-1}, respectively, a median value of 4.93 g·m^{-2}·day^{-1} and a standard deviation of ± 448.62 g·m^{-2}·day^{-1}. Soil temperatures were between 7.0 and 83.7 °C, with an arithmetic and a geometric mean of 21.19 and 19.05 °C, respectively, a median value of 17.40 °C and a standard deviation of ± 12.36 °C.

From the histogram in Fig. 5a, the soil CO_2 flux values approximately resemble a (log)normal distribution that can be correlated to a single statistical population as confirmed by the absence of clear inflection points in the cumulative frequency plot. However, even in this case, at the lowest levels the curve shows a scattered shape making uncertain the presence of inflection points. The only outlier is represented by the highest value measured in the investigated areas, i.e. 4,425.10 g·m^{-2}·day^{-1}.

In the frequency plot of Fig. 5b, the soil temperature dataset seems to show a polymodal distribution. According to the boxplot, temperatures >28.9 °C (i.e. 12 values) can be regarded as outliers of the distribution and from the cumulative frequency plot a clear inflection point can be traced at the 88.7th percentile (i.e. 28.9 °C), defining that the outliers are related to a different population. The main statistical parameters of the two soil temperatures populations of the CIES are synthetized in Table 1.

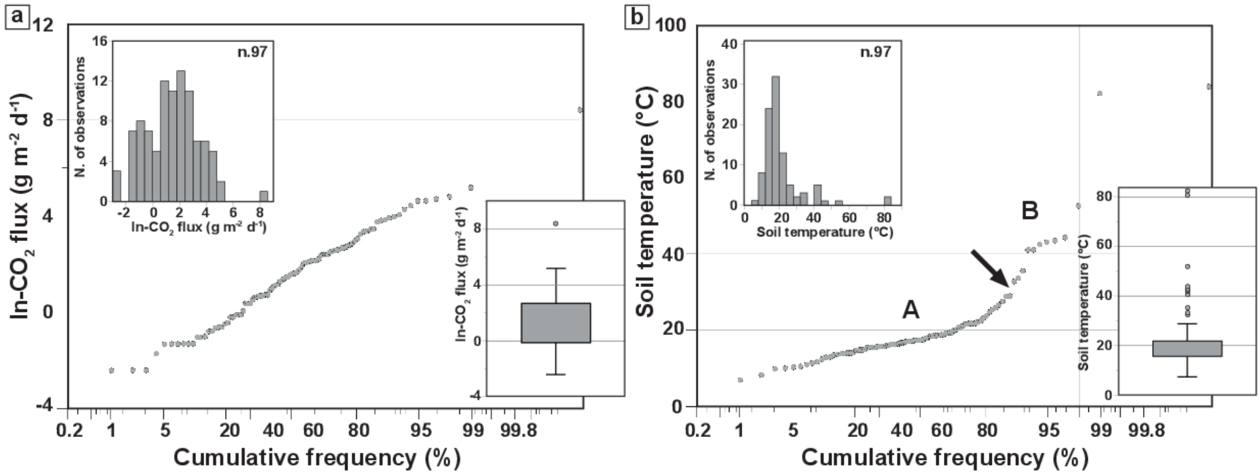

Fig. 5 - Cumulative frequency plots, histograms and boxplots of the (a) soil CO_2 and (b) temperature measurements in the Cordón de Inacaliri Eastern Sector (CIES).

Table 1. *Estimated parameters of the partitioned populations of soil temperature measurements at the CIWS and CIES*

CIWS

Population	Measurements (no.)	Temperature (°C)	Frequency	Arithmetic mean (°C)	Geometic mean (°C)	Median (°C)	St. dev. (°C)
A	201	1.6 - 38.3	93.1%	21.70	19.65	22.00	± 8.09
B + outliers	15	38.3 - 80.3	6.9%	51.72	50.33	44.90	± 13.12
Total	**216**	**1.6 - 80.3**	**100.0%**	**23.78**	**20.98**	**23.10**	**± 11.43**

CIES

Population	Measurements (no.)	Temperature (°C)	Frequency	Arithmetic mean (°C)	Geometic mean (°C)	Median (°C)	St. dev. (°C)
A	85	7.0 - 28.9	87.6%	17.42	16.84	17.10	± 4.45
B + outliers	12	28.9 - 83.7	12.4%	47.91	45.68	42.70	± 17.14
Total	**97**	**7.0 - 83.7**	**100.0%**	**21.19**	**19.05**	**17.40**	**± 12.36**

5.3 CO_2 output

The total CO_2 output of both investigated areas was calculated by applying the Sichel's t-estimator (Mi) (David, 1977), which is a reliable estimator of the total CO_2 output, especially when the CO_2 flux data are characterized by a single log-normally distributed population (Elío et al., 2016). The CO_2 output estimated with this method was derived by multiplying M_i times the area covered by the populations. In the same way, the central 95% confidence intervals of the CO_2 output were used to calculate the uncertainty of the populations. The three outliers of the two investigated sectors (i.e. the CO_2 flux values >670 g·m^{-2}·day^{-1}) were added, considering the flux over an area corresponding to the metal cylindrical vessel (i.e. 0.0314 m^2). The total computed emission rate from CIWS was 0.28 t d^{-1} (95% confidence interval 0.21 - 0.40 t d^{-1}), plus 0.05 t d^{-1} from the two outlier values recorded in this area. The CO_2 output from CIES was 0.06 t d^{-1} (95% confidence interval 0.04 - 0.11 t d^{-1}), with an additional 0.14 t d^{-1} emitted from the outlier value of the modeled area.

The computed total amount of CO_2 released through diffuse degassing from CIWS and CIES is ~0.53 t d^{-1}, distributed over a total modeled area of ~0.0179 km^2.

6. Discussion

6.1 Considerations on the soil CO_2 flux origin

The occurrence of a single population of soil CO_2 fluxes in the two investigated sectors of the CIVC was revealed by the cumulative probability plots of Figs. 4a and 5a, allowing to assess that a single generating process is apparently regulating the carbon dioxide emission. Moreover, on the basis of proximity of CIES and CIWS, the same volcano-tectonic setting and the hydrothermal and mineralogical evidences (Figs. 2 and 3), the CO_2 emissions from both areas can be assumed as governed by the same geological/geochemical processes. No carbon isotopic analyses of the diffuse gas are available and, consequently, the carbon dioxide source cannot unequivocally be defined (Cardellini et al., 2003; Chiodini et al., 2008; Hanson et al., 2014; Venturi et al., 2017). Nevertheless, some geochemical and geothermal considerations can be done.

Populations characterized by low values are mostly ascribed to natural bacterial activity and soil respiration derived from the vegetation (Viveiros et al., 2010). Vegetated areas are practically absent or represented by rare small shrubs (Fig. 3). Previous studies on similar environments (i.e. high-altitude arid geothermal/volcanic areas), such as the Cerro Pabellón geothermal area, the Juncalito geothermal prospect and the Socompa volcano (Fig. 1), and the desert scrubs areas from Utah and New Mexico (USA), assessed background (i.e. biological) values between ~1.0 and ~2.6 g·m^{-2}·day^{-1} (Raich and Schlesinger, 1992; Navarrete-Calvo, 2012; Raco, 2018; Taussi et al., 2019a). From the cumulative probability plots (Figs. 4a and 5a), no clear inflection points are recognized close to such low flux values, although scattered patterns possibly related to the closeness of the instrument detection limit, can be highlighted. The registered mean values are much higher than the supposed background value for this kind of environment. Effects due to the atmospheric conditions able to affect soil CO_2 measurements can likely be ruled out since during the field work the weather was dry and stable. In fact, barometric pressure and air temperature exhibited small variations with no correlation with the measured fluxes (Fig. 6a). Thus, the measured CO_2 fluxes in the investigated areas are necessarily to be fed by an endogenous (i.e. hydrothermal and/or volcanic) source, which likely adds to a biological source. In fact, it is worth mentioning that the scattered pattern of the cumulative frequency plot (Figs. 4a and 5a) at the lowest values of CO_2 fluxes may mask the low biological contribution, the latter being probably related with microbial communities inhabiting soil in hydrothermal diffuse degassing areas (e.g. Venturi et al., 2019) rather than soil respiration derived from the vegetation (Azua-Bastos et al., 2017).

6.2 Spatial distribution of soil CO_2 flux and temperature

Similarly to what assessed for the soil CO_2 fluxes, the mechanisms that regulate the soil temperatures in both areas can be considered analogous. As previously shown, the cumulative probability plot of the soil temperature measurements (Figs. 4b and 5b) indicates the presence of two populations for both areas, suggesting that temperatures are likely to be driven by different physical processes.

Similar soil temperature values were calculated at CIWS and CIES (Table 1), with the mean values of population A markedly higher than the mean atmospheric temperature registered during the December 2017 survey (i.e. ~12.5 °C). Considering that shallow temperatures can be influenced by different factors (e.g. atmospheric temperatures, solar insolation, rock emissivity and daytime heating; Olmsted and Ingebritsen, 1986; Lopez et al., 2018), we compared them with the air temperatures measured in each sampling site (Fig. 6a). A general low influence can be highlighted. Only the lowest values (i.e. values <~10 °C) seems to argue for ground-atmosphere temperature coupling, allowing to define that the CIWS and CIES soil temperatures can mostly be ascribed to a high geothermal gradient derived from high-enthalpy fluids at depth. In fact, the maximum values registered were 80.3 and 83.7 °C (at CIWS and CIES, respectively), i.e. near the boiling point of water (~84 °C) at this altitude (i.e. 5,150-5,200 m a.s.l.).

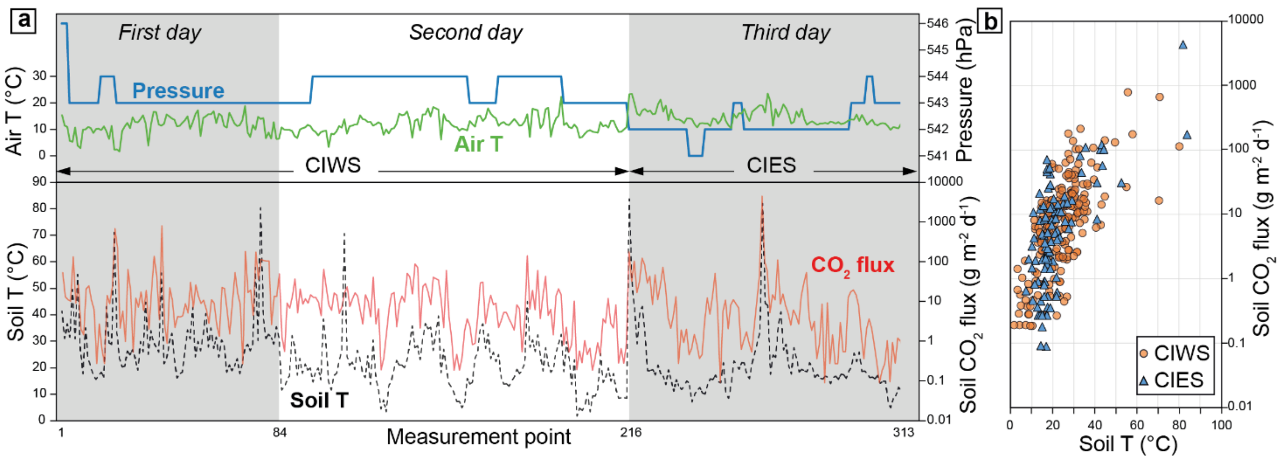

Fig. 6 - a) Correlation plot of the atmospheric parameters (air temperature and pressure) with the diffuse soil CO_2 flux and temperature during the three days of survey in both investigated areas. b) Relationship between soil CO_2 and temperature (CIWS: Cordón de Inacaliri Western Sector; CIES: Cordón de Inacaliri Eastern Sector). A positive trend seems to be highlighted.

According to Fig. 6b, diffuse CO_2 flux and soil temperatures in the Inacaliri areas seem to follow a positive trend, likely indicating that CO_2 can be coupled with rising steam. Positive correlations between soil CO_2 emission and soil temperature were assessed by many authors (e.g. Chiodini et al., 2015; Giammanco et al., 2016; Rolleau et al., 2017). Areas of active hydrothermal circulation along deep fractures (high values of soil CO_2 flux and temperature) and those affected by the absence of superficial fractures or not connected to the surface (high CO_2 flux and relatively low temperature) can thus be distinguished (Giammanco et al., 2016).

The soil CO_2 and temperature distribution maps (Fig. 7) allow to highlight how areas characterized by high CO_2 fluxes are quite well matching those showing high temperatures, corresponding to the population B sampling points (Table 1). The latter were measured when moving toward the fluid vents (Figs. 3 and 7), suggesting that a direct link with the underlying hydrothermal system is present, able to carry large amounts of CO_2 and heat to the surface. The highest soil diffuse CO_2 and temperature values (>100 $g \cdot m^{-2} \cdot day^{-1}$ and >55 °C, respectively) in CIWS are clearly located along an ENE-striking lineament (Fig. 7a,c). Furthermore, three NW-striking structural lineaments can undoubtedly be identified by both the CO_2 fluxes and temperatures in the distribution maps of Fig. 7a,c. These NW-striking lineaments coincide with the southern fault scarp of the Pabelloncito graben that dips between 50° and 70° (Tibaldi and Bonali, 2018).

At CIES, three main areas are emphasized in the soil CO_2 flux and temperature maps (Figs. 7b,d), characterized by values >20 $g \cdot m^{-2} \cdot day^{-1}$ and >~28 °C (i.e. the population B values of the CIES), respectively: two of them are located in the westernmost part, where centimetric-to-metric fluid vents (Fig. 3b,c) are possibly correlated to a NS-striking structural feature. The presence of outcropping lavas did not allow to extend our observations to a larger sector.

The positive trend between the highest values of both CO_2 flux and soil temperatures (Figs. 6b and 7) could be thus regarded as representative of areas dominated by a combination of diffusive-advective fluxes, where hydrothermal gases are primarily transported to the surface by a pressure-driven viscous flow. In fact, these areas are mostly characterized by values comprised between ~30-300 $g \cdot m^{-2} \cdot day^{-1}$ (Fig. 7a,c), in agreement with the range proposed by Rissmann et al. (2012) for this kind of transport mechanism. On the other hand, important pervasive clayey acid-sulphate hydrothermal alteration is likely responsible of the relatively wide variability observed in terms of CO_2 flux values, commonly characterized by values <30 $g \cdot m^{-2} \cdot day^{-1}$ (Fig. 7a,c) and thus referable to a purely diffusive gas transport (Rissmann et al., 2012), which is coupled with lower soil temperature values (i.e. population A). This is possibly due to different soil permeability, which could have experienced self-sealing processes, a common feature in hydrothermal system (e.g. Facca and Tonani, 1967; Fulignati et al., 1996; Hochstein and Browne, 2000), limiting the transport of the gas far from the main fractured areas (Finizola et al., 2003). Finally, it is worth to note that the lowest soil temperature values (i.e. values <~10 °C) are mainly located in the southern part of the CIWS and could possibly define the border of the degassing structure (Fig. 7c), being also related to low values of CO_2 fluxes (i.e. <~1 g·m^{-2}·day^{-1}; Fig. 7a).

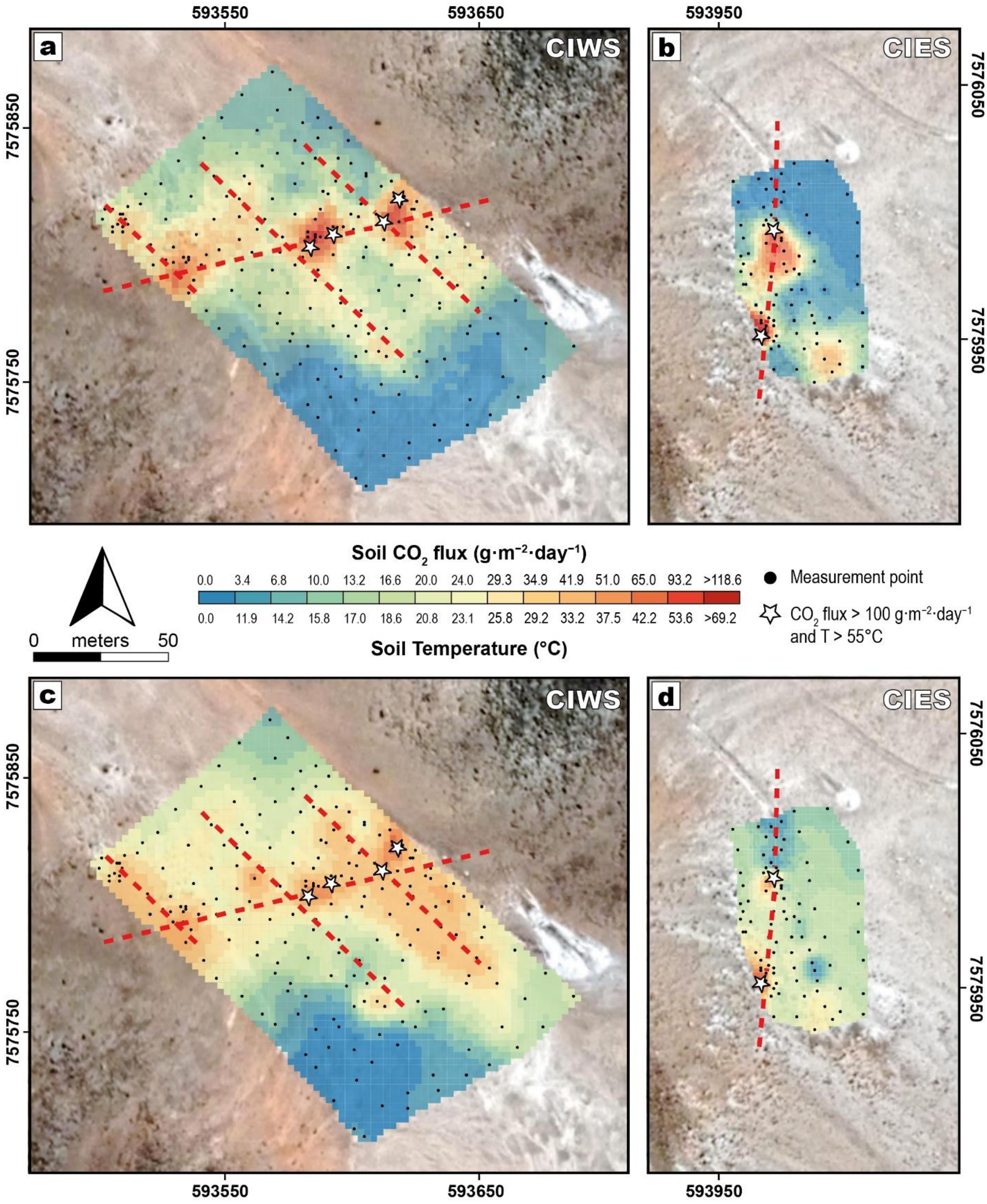

Fig. 7 - a-b) Distribution maps of soil CO_2 flux and c-d) soil temperature at 10 cm depth at CIWS and CIES. Black dots: measurement points; white stars: sites where CO_2 flux and temperature were higher than 100 g·m^{-2}·day^{-1} and 55 °C, respectively. The inferred structural lineaments (red dashed

lines) are also highlighted. Semivariograms and cross-validations of each map are reported in the Supplementary Material S2.

6.3 Structural control on the fluid emissions

From the geological (Fig. 2) and the planar and perspective (Fig. 8) maps, two NW-striking normal faults, recognized inside the Pabelloncito graben, with an arcuate trace in the planar view, consistent with a gentle dip, are located close to the study area. These two lineaments form antithetic subsidiary faults that are parallel to the southern main fault of the Pabelloncito graben (Fig. 8b). Between these lineaments, an ENE-striking linear feature seems to be defined by both the spatial distribution of soil CO_2 and temperature (Fig. 7), and volcano-morphometric indicators (e.g. orientation of crater/eruptive centre elongation; see Tibaldi, 1995 for further details), the latter being useful to identify possible shallow magma-feeding fractures (Tibaldi et al., 2017). The highest soil CO_2 fluxes and the population B of the soil temperatures in the CIWS are distributed along an ENE-striking lineament (Fig. 7). Additionally, an interposed small dome-like morphological structure, which shows a clear ENE elongation (Figs. 3a and 8a), occurs between the CIWS and CIES and is coupled with a >600 m long ENE-striking ridge (i.e. to the East of CIES; Figs. 3a,f). This suggests that this lineament is not confined to the border of the Pabelloncito graben, but it continues toward the central sectors. All the active (i.e. the main hydrothermal vents from both areas; Fig. 3) and relict thermal features are located at the intersection between the NW- and ENE-striking lineaments, highlighting a critical role of both structures in the discharge of hydrothermal fluids and lavas (Fig. 8a). Intersecting linear structures with similar orientations have also been observed in other geothermal/volcanic systems of the Central Andes, e.g. Tocomar (Giordano et al., 2013) and Sol de Mañana (Haffen et al., 2020) geothermal fields, and the fumarolic field of the AAVC (Taussi et al., 2019a). These observations are consistent with structures forming a transfer fault zone, in the sense of Faulds and Hinz (2015), which exerts a primarily control on the migration of thermal fluids towards the surface. High-permeability fracture pathways, often associated with the intersections of tectonic features, are well-known to form conduits in hydrothermal systems for the transport of mass and energy (e.g., Curewitz and Karson, 1997; Fairley and Hinds, 2004; Werner and Cardellini, 2006; Faulds and Hinz, 2015; Jolie et al., 2015), and this behaviour is shown by the high temperatures and CO_2 fluxes observed in our study area at the intersections of the structural lineaments (Fig. 7). Another interesting feature is the occurrence of a presently inactive fumarole East of the CIES (Figs. 3f and 8). This suggests that the center of hydrothermal activity has migrated over time, possibly as the result of hydrothermal alteration affecting this sector of the Pabelloncito graben (Figs. 2, 3 and 8), with the subsequent reduction of permeability (e.g. Curewitz and Karson, 1997)

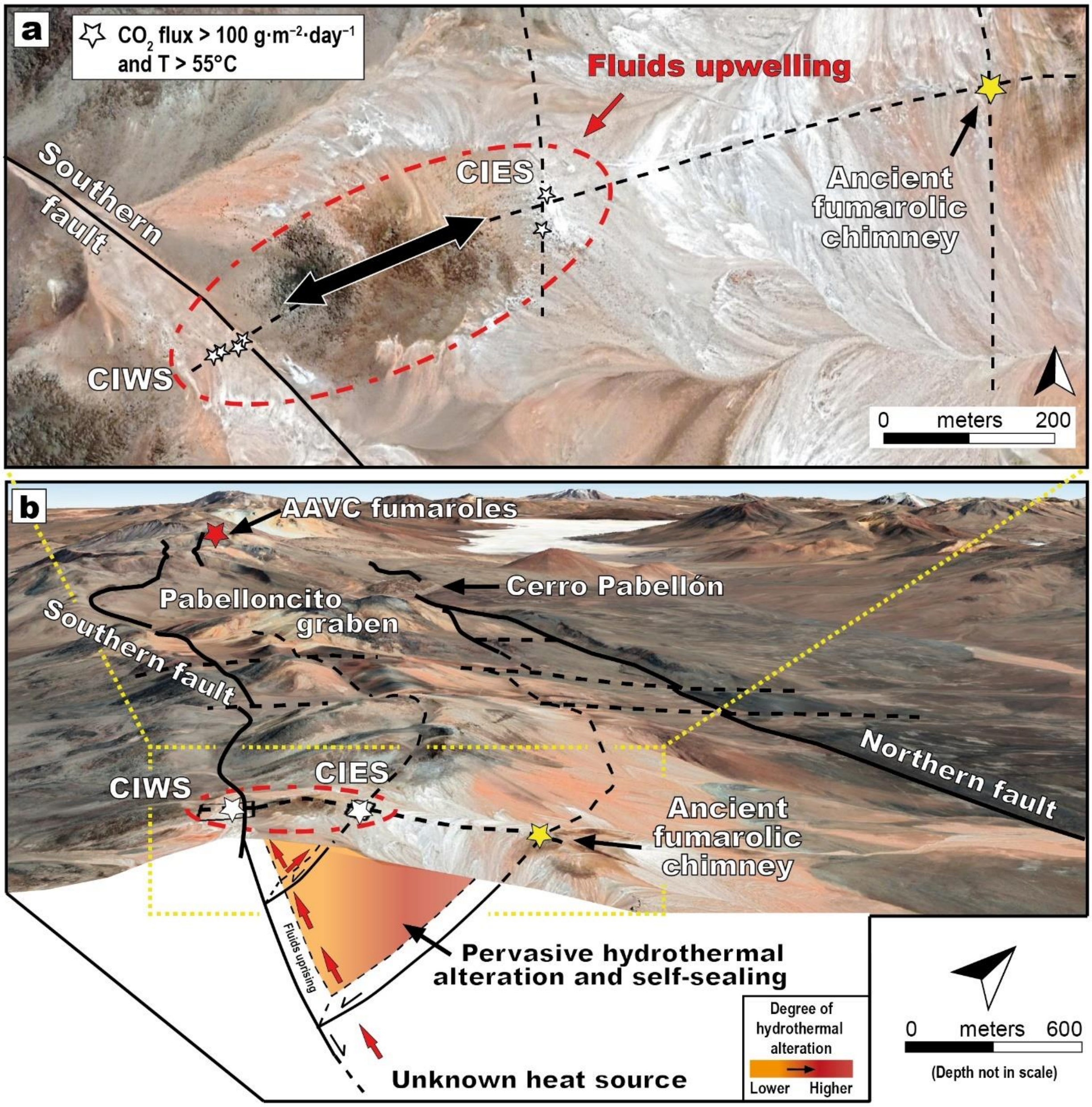

Fig. 8 - a) Planar view of the studied area highlighting the main geochemical (white stars) and morphometric (ENE-elongated dome-like morphological structure) features that clearly indicate the presence of two intersecting tectonic lineaments that favour the fluids upwelling. The black double arrow indicates the elongation direction of the dome-like morphological structure. The main structural lineaments are reported in black (dashed when uncertain) after Sellés and Gardeweg (2017). b) Perspective view of the investigated area and Pabelloncito graben, up to Cerro Pabellón geothermal site and the Apacheta-Aguilucho Volcanic Complex (AAVC). CIWS and CIES are located along the intersections between the NW- and the ENE-striking lineaments, which also include the remnants of a fumarolic chimney (yellow star). It is worth to note that the active thermal manifestations (white stars) of the Cordón de Inacaliri and AAVC hydrothermal systems (red star) are located close to the Pabelloncito southern fault.

6.4 Diffuse soil CO_2 output

The total computed diffuse soil CO_2 output from the Cordón de Inacaliri investigated sectors resulted to be ~0.53 t·d^{-1}, distributed over an area of ~0.0179 km^2. Although the absolute value of endogenous emissions from the Cordón de Inacaliri system is relatively low compared to other geothermal areas worldwide (e.g. ~12 t d^{-1} for the Reykjanes area in Iceland; Fridriksson et al., 2006), the level of the normalized total CO_2 flux from soil (total flux divided by the area of the survey) is ~29.6 t·d^{-1}·km^{-2}, which is comparable to the endogenous emissions of other geothermal and/or volcanic areas in Central and South America and worldwide (Table 2 and Fig. 9).

Table 2. Soil CO_2 output from the Cordón de Inacaliri hydrothermal system compared with other geothermal and volcanic sites worldwide.

Site	Country	Area (km^2)	Endogenous diffuse CO_2 output (t d^{-1})	Normalized CO_2 output (t d^{-1} km^{-2})	Reference
Cordón de Inacaliri	*Chile*	*0.0179*	*0.53*	*29.6*	*This work*
Lastarria	Chile	0.039	5.0	129.1	Lopez et al., 2018
Copahue	Argentina	1.213	212.7	175.4	Chiodini et al., 2015
Cuicocha	Ecuador	13.3	106	8.0	Padrón et al., 2008
Pululahua	Ecuador	27.6	270	9.8	Padrón et al., 2008
La Escalera	Mexico	0.008	0.62	76.3	Jácome-Paz et al., 2019
Agua Caliente	Mexico	0.01	0.498	49.3	Jácome-Paz et al., 2019
Los Humeros	Mexico	0.50	26.10	52.2	Jentsch et al., 2020
El Tizate	Nicaragua	1.46	64	44	Ostapenko et al., 1998
Krafla	Iceland	0.63	14.0	22.2	Dereinda, 2008
Reykjanes	Iceland	0.225	12.0	53.3	Fridriksson et al., 2006
Nisyros	Greece	2.22	91.6	41.3	Bini et al., 2019
Mount Amiata	Italy	225	8529	37.9	Sbrana et al., 2020
Latera	Italy	3.1	350	112.9	Chiodini et al., 2007
Ischia, Donna Rachele	Italy	0.06	10	173	Chiodini et al., 2004
Yangbajain	Tibet, China	3.2	138	43.1	Chiodini et al., 1998
Karapiti, Wairakei	New Zeland	0.35	6.0	17.1	Werner et al., 2004
Rotorua	New Zeland	8.9	620	69.7	Werner and Cardellini, 2006

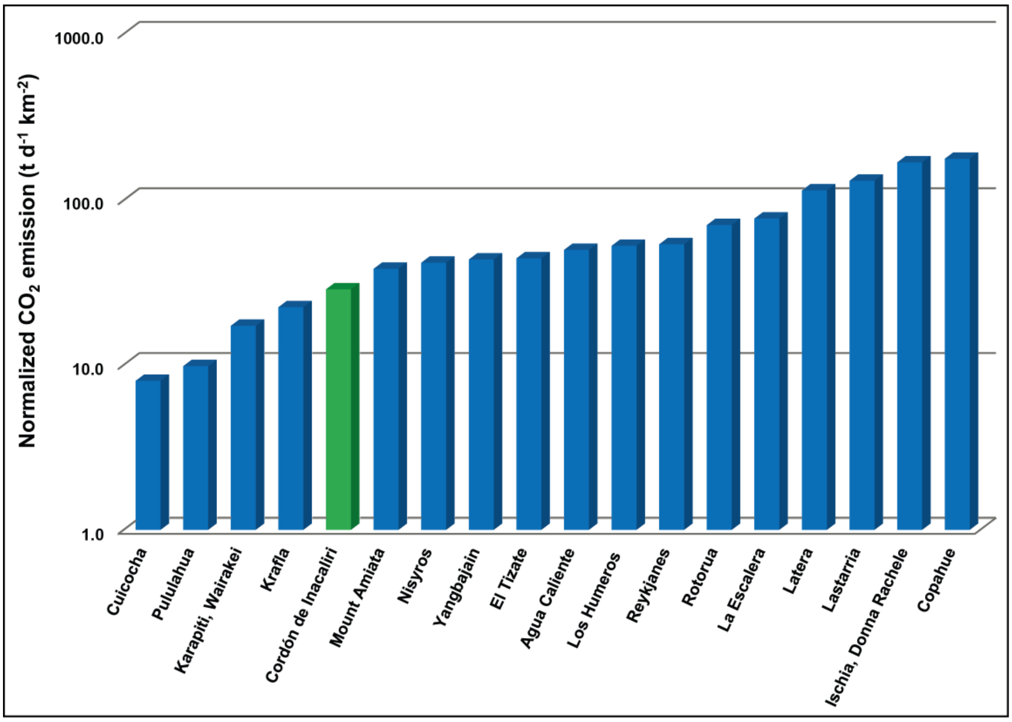

Fig. 9 - Plot of the normalized CO_2 diffuse emissions for the Cordón de Inacaliri hydrothermal system compared with selected worldwide geothermal systems and volcanic areas (see Table 2 for references).

6.5 Heat flux estimates

Theoretical expressions for estimating heat flux from shallow ground temperature measurements have been published by many authors through the years (e.g. Dawson, 1964; Olmsted and Ingebritsen, 1986; Sorey and Colvard, 1994; Hochstein and Bromley, 2005; Hurwitz et al., 2012; Price et al., 2017). Some of these required many input data to properly determine the heat flux. For examples, Olmsted and Ingebritsen (1986) found an empirical correlation between soil temperatures from boreholes at 30 m depth and heat flow units. Hochstein and Bromley (2005) computed the heat flux from soil temperature gradients, while Hurwitz et al. (2012) coupled these latter with laboratory analyses and the chloride inventory method to define the heat flow in two vapor dominated, acid-sulphate thermal areas of Yellowstone (USA). Price et al. (2017) used shallow soil temperatures coupled with seismic refraction and physical properties of the thermal discharges to construct a model for the advective transport of heat energy in hydrothermal fluids that incorporated heat exchange with the surroundings. Instead, the approach proposed by Dawson (1964) (modified by Sorey and Colvard, 1994) estimates the total heat flux from steaming ground through empirical correlations, only considering shallow soil temperature at 15 cm of depth. This methodology was used to estimate the heat flux and the geothermal potential at the CIVC studied area. The measured shallow soil temperatures were converted to equivalent heat flux values following the modified empirical procedure of Dawson (1964), which measured the surface heat flux using a water-filled calorimeter and empirical power law functions were then derived to convert shallow soil temperatures to equivalent heat flux values. The method was originally applied to shallow soil temperatures measured in specific thermal areas from the Wairakei geothermal field (New Zealand), but it was also extended to different environments such as Lassen Volcanic National Park (U.S.A.; Sorey and Colvard, 1994), Hengill volcanic system (Iceland; Hernández et al., 2012) and Teide volcano (Spain; Alonso et al., 2019). At CIVC, temperature measurements were performed at the slightly shallower depth of 10 cm, consequently, the converted heat flux values are expected to be underestimated (Bloomberg et al., 2014). The Dawson's (1964) original equation is the follow:

$$q = 5.2 \times 10^{-6}\ t_{15}^{4} \qquad (1)$$

where q is the heat flux (W m^{-2}) at the soil surface, 5.2×10^{-6} is the empirical constant (in W m^{-2} /°C) and t_{10} is the soil temperature at 15 cm depth (in °C). The Dawson (1964) approach derived from thermal surveys carried out at low altitude terrains (i.e. ~400 m a.s.l. and boiling point of water ~98.5 °C), but it was then slightly modified by Sorey and Colvard (1994) using a revised constant of 6.7 x 10^{6} to account for the change of the boiling point of water with elevation (i.e. ~93 °C at 2,500 m a.s.l.). The procedure to obtain the corrected value was not defined by Sorey and Colvard (1994). Thus, a linear correlation between decreasing temperature of boiling water with increasing altitude was considered and a coefficient of 9.15 x 10^{-6} for the conditions of the present study was computed. The surface heat flux was thus calculated according to the following equation:

$$q = 9.15 \times 10^{-6}\ t_{10}^{4} \qquad (2)$$

Steam flux can be inferred by assuming the measured heat flux results from the sum of (i) condensation of steam in the shallow sub-surface (conductive heat flux), and (ii) convective steam flux (Brombach et al., 2001; Werner et al., 2004; Hochstein and Bromley, 2005; Fridriksson et al., 2006; Rissmann et al., 2012; Harvey et al., 2017) as follow:

$$F_{stmq} = q_m \times a \times (H_{V,85\,°C} - H_{L,12°C})^{-1} \qquad (3)$$

Where F_{stmq} is the steam flux (kg s^{-1}), q_m is the arithmetic mean thermal ground heat flux (converted in kJ m^{-2} s^{-1}) derived from Eq. (2), a is the investigated area (in m^2), $H_{V,85\,°C}$ is the enthalpy of steam at 85 °C (i.e. ~ the boiling point of water at the CIVC altitude) and $H_{L,12°C}$ is the enthalpy of liquid water at the mean ambient temperature recorded during the December 2017 survey (2651.5 kJ/kg and 50.4 kJ/kg, respectively; Rogers and Mayhew, 1995). The resulted q_m value is 1.08x10^{-2} kJ m^{-2} s^{-1} (i.e. 10.84 W m^{-2}), with the minimum and maximum values ranging from <1x10^{-4} to 0.449 kJ m^{-2} s^{-1} (i.e. 6x10^{-5} and 449 W m^{-2}), respectively (Supplementary Material S1). When steam condensation within the soil is the dominant heat transfer mechanism (Rissmann et al., 2012), the mass flow of steam (F_{stmq}) is 0.075 kg s^{-2} (i.e. 6.45 t d^{-1} of steam). This value corresponds to a total heat flow rate of ~0.2 MW and a total heat flux of ~10.8 MW km^{-2}. Based on the total amount of steam and CO_2 release, a CO_2/H_2O ratio of 0.08 was calculated. Anyway, it is worth to note, that the results based on Eq. (3) might be slightly overestimated (McMillan et al., 2018).

To compare our results of the heat flux with similar geological contexts, the same approach was applied to the AAVC fumarolic field, situated ~12 km NW from the studied area. Both areas are Pleistocene in age (Sellés and Gardeweg, 2017) and are located in i) an analogous altitude (i.e. ~5,150-5,200 m a.s.l.) and ii) the same tectonic structure (i.e. Pabelloncito graben; Fig. 2). In addition, they are characterized by i) similar hydrothermal mineral assemblages at the surface (Hubbard and Crowley, 2005; Maza et al., 2018b; Morata et al., 2020b), ii) intermediate to acid volcanic rocks (i.e. andesites to rhyolites; Piscaglia, 2011; Taussi et al., 2019b) and iii) relatively high soil temperatures (Taussi et al., 2019a). The atmospheric and soil temperatures measured at 10 cm of depth from the AAVC fumarolic field (Taussi et al., 2019a) were used to estimate the heat flux at the soil surface according to Eq. (2). The resulted mean heat flux is 0.065 kJ m^{-2} s^{-1} (i.e. 64.87 W m^{-2}) with minimum and maximum values ranging between <1x10^{-4} and 0.441 kJ m^{-2} s^{-1} (i.e. 0.02 and 441 W m^{-2}) (Supplementary Material S1). The mean heat flux was then applied to Eq. 3, over an area of ~16,300 m^2, obtaining $H_{V,85\ °C}$ = 2651.5 kJ/kg and $H_{L,8ºC}$ = 33.6 kJ/kg (i.e. the enthalpy of liquid water at ~7.5 °C, that is the mean ambient temperature recorded by Taussi et al., 2019a in November 2016). The mass flow of steam (F_{stmq}) is 0.40 kg s^{-2} (i.e. 34.90 t d^{-1} of steam) corresponding to a total heat flow rate of ~1.2 MW and a total heat flux of ~71.2 MW km^{-2}.

It is worth to mention that the CO_2/H_2O ratio at CIVC (0.08) is slightly higher than that of the AAVC (i.e. ~0.02 and ~0.01; Urzua et al., 2002 and Tassi et al., 2010, respectively) and much lower than those from other geothermal systems of the Central Andes (i.e. >~3.5; see Tassi et al., 2010 for further details), whereas it approaches that of El Tatio geothermal field (i.e. ~0.11-0.16; Tassi et al., 2010).

6.6 Geothermal potential

A low total CO_2 emission output as that calculated in the CIVC (i.e. 0.53 t d^{-1}) is not necessarily related to a small geothermal system. High CO_2 fluxes and CO_2/H_2O ratios often characterize vapour core systems (Fig. 10) resulting from a degassing magma at depth, where no deep liquid reservoir is present to remove CO_2 during ascent (Harvey et al., 2015). This contrasts with liquid-dominated systems, where a greater proportion of the ascending CO_2 can be dissolved in the reservoir liquid or precipitate (Harvey et al., 2015). At the CIVC the CO_2/H_2O ratio lies between the lowest values of vapour core systems and the highest of the liquid dominated ones (Fig. 10). Also El Tatio and the AAVC fumarolic field (which is the only surface manifestation of the Cerro Pabellón geothermal system) are characterized by comparable CO_2/H_2O ratios and are both related to liquid-dominated geothermal systems (Cortecci et al., 2005; Tassi et al., 2010). In this way, similar conditions can be envisaged for the CIVC geothermal reservoir where a liquid dominated system can be inferred as well.

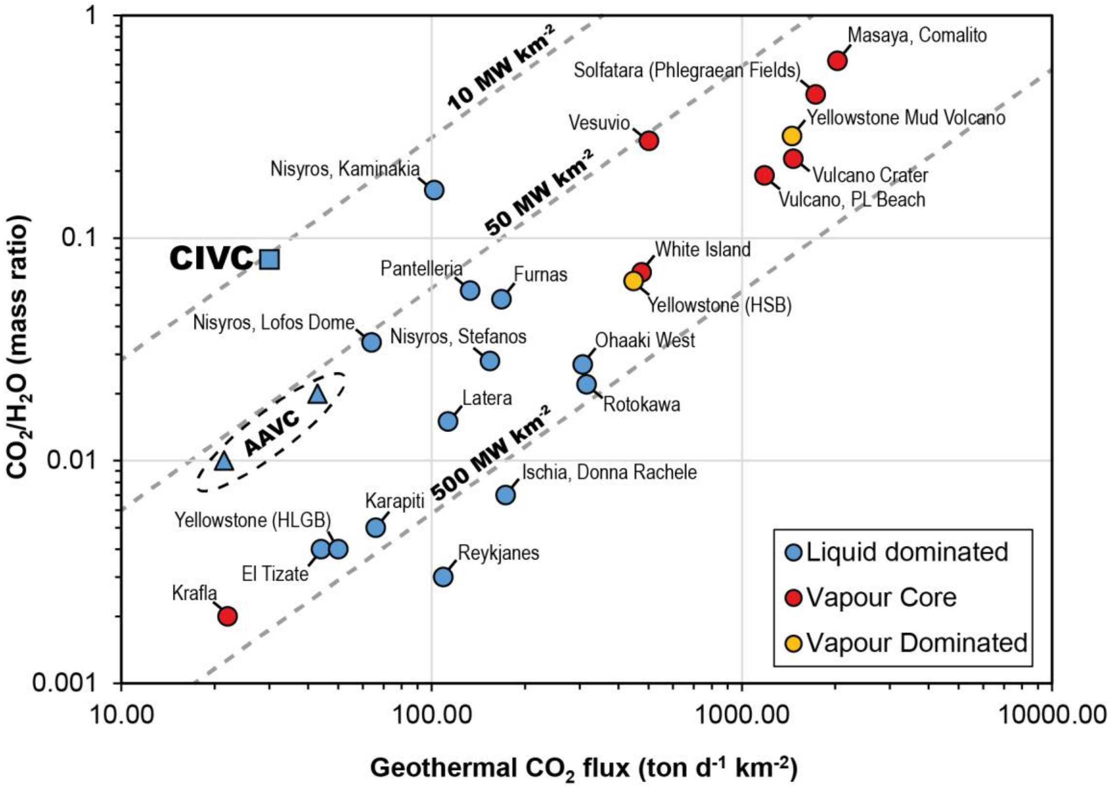

Fig. 10 - CO_2/H_2O versus log mean CO_2 flux for hydrothermal systems (data from Harvey et al., 2015 and references therein). The CIVC show a normalized CO_2 output comparable with other liquid-dominated systems and a CO_2/H_2O ratio higher than most of these latter systems. Dashed grey lines represent the heat flux isolines at 10, 50 and 500 MW km^{-2} respectively.

Being assessed that the normalized output per km^{-2} is comparable with that of other geothermal systems worldwide (Table 2; Fig. 9), another interesting feature that could influence the total CO_2 discharge output is the presence of a pervasive and intense hydrothermal mineralogical alteration that characterizes the studied area (Figs. 2 and 3). In fact, a pervasive hydrothermal alteration might avoid a high flux of fluids to be discharged at surface, similarly to what happen in the nearby Cerro Pabellón, where a thick and impermeable clay-cap maintains the geothermal fluids at depth preventing hydrothermal manifestations at the surface (Maza et al., 2018a; Taussi et al., 2019a). Therefore, it is not possible to exclude that a hidden geothermal system could be located towards E of the studied area, in those sectors of the graben where the oldest hydrothermal activity could have been able to produce an efficient clay-cap (or cap-rock), favouring the migration of the surface hydrothermal activity toward W (Fig. 8). In this way, the investigated areas of this work would possibly represent the present-day high temperature surface expression of the CIVC hydrothermal system, similarly to what occurs for the AAVC fumarolic field linked to the Cerro Pabellón geothermal system. The differences in the heat fluxes recognized between the CIVC and the AAVC fumarolic field are likely related to the older age of the volcanic activity of the former (i.e. between 1.6 and 1.0 Ma; Sellés and Gardeweg, 2017) with respect to the latter where the presence of a still-active hydrothermal system associated with significant quantities of magmatic gases was evaluated by Tassi et al. (2010).

Finally, a rough value of 1.08 MW electric km^{-2} would be expected assuming a typical conversion efficiency of 0.1 from thermal to electric energy (Zarrouk and Moon, 2014; Harvey et al., 2015), related to conventional geothermal power plants. Although no indications about the extension of the reservoir of the CIVC geothermal system are presently available, the horizontal extension of the reservoir of the Cerro Pabellón geothermal system was estimated between 4 and 25 km^2 and comprised within the faults of the Pabelloncito graben (Aravena et al., 2016). Assuming analogous conditions for the CIVC geothermal reservoir, a capacity between 4.3 and 27.0 MWe is estimated.

7. Conclusions

A geothermal investigation of the hydrothermally altered area in the Chilean Cordón de Inacaliri Volcanic Complex was performed for the first time. Soil CO_2 and temperature measurements were carried out with the aim to assess the structural control on the rising fluids, the total CO_2 output and the geothermal potential of this unexplored site. The survey was conducted across two areas of about 0.0179 km^2 in the southern part of the NW-striking Pabelloncito graben, where an extensive and pervasive hydrothermal mineralogical alteration is present at the surface. CO_2 flux values of up to ~4,400 g m^{-2} d^{-1} and temperature near the boiling point of water at this altitude (i.e. ~84 °C) were measured, likely associated with an endogenous source.

From the diffuse CO_2 and temperature distribution maps, a clear ENE-striking anomaly was highlighted. This evidence is strengthened by the presence of a small dome-like morphological structure outcropping between the two investigated sub-areas (CIWS and CIES) and by a >600 m long ridge, both elongated ENE. The presence of two antithetic subsidiary faults, parallels to the southern main fault of the Pabelloncito graben, coupled with the ENE-striking lineament (Fig. 8b) forms a favourable structural setting for fluid flow, driven by a transfer fault zone. In fact, the main active and ancient hydrothermal features are located along the intersections of the NW- and ENE-striking lineaments (Fig. 8), where the highest soil CO_2 and temperature values, likely associated to a combination of diffusive-advective transport mechanism, were measured. This suggests that the two tectono-morphological lineaments play a fundamental role in controlling the ascent of the hydrothermal fluids.

Soil temperatures were used to calculate the heat flow rate and heat flux from the CIVC hydrothermally altered area, resulting in ~0.2 MW and ~10.8 MW km^{-2}, respectively. Converting thermal to electric energy, 1.08 MW electric km^{-2} would be expected. No data about the size of the reservoir are available but considering similar conditions to the Cerro Pabellón geothermal system, a total electric energy potential of 4.3-27.0 MWe is estimated. The total CO_2 output from the CIVC hydrothermal system is not high in terms of absolute values (i.e. ~0.53 t d^{-1}), but the normalized output per km^2 (i.e. ~29.6 t d^{-1} km^2) and the CO_2/H_2O ratio (i.e. 0.08) suggest that a liquid dominated geothermal reservoir could be present at the CIVC, being both parameters comparable with some of the main geothermal system worldwide.

Soil temperatures up to the local boiling point of water and the heat flux, coupled with fluids driven by the presence of favourable tectono-volcanic structures, make this part of the Pabelloncito graben a good candidate for future geothermal exploration studies. In fact, even if located in a remote area, the CIVC hydrothermal field is only ~9 km away from the Cerro Pabellón geothermal power plant, which is currently producing electricity. The presence of infrastructures (i.e. roads and transmission line) represents an optimistic issue to overcome the critical problems that could limit the development of geothermal energy production, such as distance to the main electricity network, high elevation and operational logistics (Sanchez-Alfaro et al., 2015). Further surface exploration studies involving volcanology, petrology, fluids geochemistry and structural analyses, are however needed to assess the exploitability of this geothermal area. Detailed mineralogical studies on the main hydrothermal alteration facies and gas geochemistry and isotopes (e.g. $\delta^{13}C$-CO_2 and $^3He/^4He$) from fluids vents and diffuse emissions at CIVC are to be scheduled in order to better constrain the source of the hydrothermal fluids, also for a more effective comparison with the Cerro Pabellón hidden geothermal system.

Acknowledgments

This work has been carried out in the frameworks of a collaboration with Enel Green Power and the Memorandum of Understanding between the Department of Pure and Applied Sciences (DiSPeA) of the University of Urbino and the Faculty of Physical and Mathematical Sciences of the Universidad de Chile. The investigation was financially supported by the University of Urbino through a PhD grant to M. Taussi, and the ANID-FONDAP project 15090013 (Andean Geothermal Center of Excellence, CEGA). We are grateful to Guido Cappetti (Enel Green Power) for encouraging this research and facilitating the fieldwork in the Cordón de Inacaliri area. Fr. Aguilera and Dr. B. Godoy (CEGA) and Carlos Ramírez (Enel Green Power) are thanked for their help and assistance during fieldwork. The Authors wish to express their gratitude to C. Bromley, J. Fairley, and M. Procesi for their useful and insightful suggestions and comments that significantly improved an early version of the manuscript.

References

1. Alonso, M., Padrón, E., Sumino, H., Hernández, P.A., Melián, G.V., Asensio-Ramos, M., Rodríguez, F., Padilla, G., García-Merino, M., Amonte, C., Pérez, N.M., 2019. Heat and Helium-3 Fluxes from Teide Volcano, Canary Islands, Spain. Geofluids, vol. 2019, article ID 3983864, 12 pp. https://doi.org/10.1155/2019/3983864.

2. Aravena, D., Muñoz, M., Morata, D., Lahsen, A., Parada, M.A., Dobson, P., 2016. Assessment of high enthalpy geothermal resources and promising areas of Chile. Geothermics 59, 1–13. http://dx.doi.org/10.1016/j.geothermics.2015.09.001.

3. Azua-Bastos, A., González-Silva, C., Corsini, G., 2017. The hyperarid core of the Atacama Desert, an extremely dry and carbon deprived habitat of potential interest for the field of carbon science. Frontiers in Microbiology, vol. 8, 993, pp. 1-6. doi:10.3389/fmicb.2017.00993.

4. Barcelona, H., Lelli, M., Norelli, F., Peri, G., Winocur, D., 2019. Hydrochemical and geological model of the Bañitos-Gollete geothermal system in Valle del Cura, main Andes Cordillera of San Juan, Argentina. Journal of South American Earth Sciences 96, 102378. https://doi.org/10.1016/j.jsames.2019.102378.

5. Beck, S.L., Zandt, G., Myers, S.C., Wallace, T.C., Silver, P.G., Drake, L., 1996. Crustal-thickness variations in the central Andes. Geology, 24 (5), pp. 407-410. https://doi.org/10.1130/0091-7613(1996)024<0407:CTVITC>2.3.CO;2.

6. Bini, G., Chiodini, G., Cardellini, C., Vougioukalakis, G.E., Bachmann, O., 2019. Diffuse emission of CO2 and convective heat release at Nisyros caldera (Greece). Journal of Volcanology and Geothermal Research, 376, pp. 44-53. https://doi.org/10.1016/j.jvolgeores.2019.03.017

7. Bloomberg, S., Werner, C., Rissmann, C., Mazot, A., Horton, T., Gravley, D., Kennedy, B., Oze, C., 2014. Soil CO_2 emissions as a proxy for heat and mass flow assessment, Taupo Volcanic Zone, New Zealand. Geochemistry, Geophysics, Geosystems, 15, pp. 4885-4904. Doi:10.1002/2014GC005327.

8. Bona, P., Coviello, M., 2016. Valoración y gobernanza de los proyectos geotérmicos en América del Sur: una propuesta metodológica. Comisión Económica para América Latina y el Caribe (CEPAL), Copyright© United Nations; pp. 178.

9. Brombach, T., Hunziker, J.C., Chiodini, G., Cardellini, C., Marini, L., 2001. Soil diffuse degassing and thermal energy fluxes from the southern Lakki plain, Nisyros (Greece). Geophysical Research Letters, vol. 28 (1), pp. 69-72. https://doi.org/10.1029/2000GL008543.

10. Carapezza, M.L., Ranaldi, M., Gattuso, A., Pagliuca, N.M., Tarchini, L., 2015. The sealing capacity of the cap rock above the Torre Alfina geothermal reservoir (Central Italy) revealed by soil CO_2 flux investigations. Journal of Volcanology and Geothermal Research, 291, 25–34. https://doi.org/10.1016/j.jvolgeores.2014.12.011.

11. Cardellini, C., Chiodini, G., Frondini, F., 2003. Application of stochastic simulation to CO_2 flux from soil: Mapping and quantification of gas release. Journal of Geophysical Research, 108, B9, pp. 2425. http://dx.doi.org/10.1029/2002JB002165.

12. Cardellini, C., Chiodini, G., Frondini, F., Avino, R., Bagnato, E., Caliro, S., Lelli, M., Rosiello, A., 2017. Monitoring diffuse volcanic degassing during volcanic unrests: the case of Campi Flegrei (Italy). Scientific Reports, 7, 6757. Doi:10.1038/s41598-017-06941-2.

13. Chiodi, A., Tassi, F., Báez, W., Filipovich, R., Bustos, E., Glok Galli, M., Suzaño, N., Ahumada, Ma. F., Viramonte, J.G., Giordano, G., Pecoraino, G., Vaselli, O., 2019. Preliminary conceptual model of the Cerro Blanco caldera-hosted geothermal system (Southern Puna, Argentina): Inferences from geochemical investigations. Journal of South American Earth Sciences 94, 102213. https://doi.org/10.1016/j.jsames.2019.102213.

14. Chiodini, G., Cioni, R., Guidi, M., Raco, B., Marini, L., 1998. Soil CO_2 flux measurements in volcanic and geothermal areas. Applied Geochemistry, 13, 5, pp. 543-552. https://doi.org/10.1016/S0883-2927(97)00076-0.

15. Chiodini, G., Avino, R., Brombach, T., Caliro, S., Cardellini, C., De Vita, S., Frondini, F., Granieri, D., Marotta, E., Ventura, G., 2004. Fumarolic and diffuse soil degassing west of Mount Epomeo, Ischia, Italy. Journal of Volcanology and Geothermal Research, 133, pp.291-309. doi:10.1016/S0377-0273(03)00403-7.

16. Chiodini, G., Baldini, A., Barberi, F., Carapezza, M.L., Cardellini, C., Frondini, F., Granieri, D., Ranaldi, M., 2007. Carbon dioxide degassing at Latera caldera (Italy): geothermal reservoir and evaluation of its potential energy. Journal of Geophysical Research, 112, B12204, 17. doi:10.1029/2006JB004896, 2007.

17. Chiodini, G., Caliro, S., Cardellini, C., Avino, R., Granieri, D., Schmidt, A., 2008. Carbon isotopic composition of soil CO_2 efflux, a powerful method to discriminate different sources feeding soil CO_2 degassing in volcanic-hydrothermal areas. Earth and Planetary Science Letters 274, pp. 372–379. doi:10.1016/j.epsl.2008.07.051.

18. Chiodini, G., Cardellini, C., Lamberti, M.C., Agusto, M., Caselli, A., Liccioli, C., Tamburello, G., Tassi, F., Vaselli, O., Caliro, S., 2015. Carbon dioxide diffuse emission and thermal energy release from hydrothermal systems at Copahue–Caviahue Volcanic Complex (Argentina). Journal of Volcanology and Geothermal Research, 304, pp. 294-303. http://dx.doi.org/10.1016/j.jvolgeores.2015.09.007.

19. Cortecci, G., Boschetti, T., Mussi, M., Herrera Lameli, C., Mucchino, C., Barbieri, M., 2005. New chemical and original isotopic data on waters from El Tatio geothermal field, northern Chile. Geochemical Journal, vol. 39, pp. 547-571. https://doi.org/10.2343/geochemj.39.547.

20. Curewitz, D., Karson, J.A., 1997. Structural settings of hydrothermal outflow: Fracture permeability maintained by fault propagation and interaction. Journal of Volcanology and Geothermal Research, 79, pp. 149-168. https://doi.org/10.1016/S0377-0273(97)00027-9.

21. David, M., 1977. Geostatistical Ore Reserve Estimation. Elsevier Science, New York, 384 pp.

22. Dawson, G.B., 1964. The nature and assessment of heat flow from hydrothermal areas. New Zealand Journal of Geology and Geophysics, 7, pp. 155-171.

23. de Silva, S.L., 1989. Altiplano-Puna volcanic complex of the central Andes. Geology 17 (12), pp. 1102-1106. https://doi.org/10.1130/0091-7613(1989)017<1102:APVCOT>2.3.CO;2.

24. Dereinda, F.H., 2008. CO_2 Emissions from the Krafla Geothermal Area, Iceland, United Nations University Geothermal Training Programme, Reports 2008.

25. Elío, J., Ortega, M.F., Nisi, B., Mazadiego, L.F., Vaselli, O., Caballero, J., Chacón, E., 2016. A multi-statistical approach for estimating the total output of CO_2 from diffuse soil degassing by the accumulation chamber method. International Journal of Greenhouse Gas Control 47, pp. 351-363. https://doi.org/10.1016/j.ijggc.2016.02.012.

26. Facca, G., Tonani F., 1967. The self-sealing geothermal field. Bulletin Volcanologique, vol. 30, pp. 271-273. https://doi.org/10.1007/BF02597674.

27. Fariley, J.P., Hinds, J.J., 2004. Rapid transport pathways for geothermal fluids in an active Great Basin fault zone. Geology, vol. 32 (9), pp. 825-828. doi: 10.1130/G20617.1.

28. Faulds, J.E., Hinz, N.H., 2015. Favorable tectonic and structural settings of geothermal systems in the Great Basin Region,Western USA: proxies for discovering blind geothermal systems. World Geothermal Congress, Melbourne, Australia, pp. 1–6.

29. Finizola, A., Sortino, F., Lénat, J.F., Aubert, M., Ripepe, M., Valenza, M., 2003. The summit hydrothermal system of Stromboli. New insights from self-potential, temperature, CO_2 and fumarolic fluid measurements, with structural and monitoring implications. Bulletin of Volcanology, 65, pp. 486-504. https://doi.org/10.1007/s00445-003-0276-z

30. Fischer, T.P., Aiuppa, A., 2020. AGU Centennial Grand Challenge: Volcanoes and Deep Carbon Global CO_2 Emissions From Subaerial Volcanism - Recent Progress and Future Challenges. Geochemistry, Geophysics, Geosystems, vol. 21, Issue 3, article number e2019GC008690. Doi: 10.1029/2019GC008690.

31. Francis, P.W., Rundle, C.C., 1976. Rates of production of the main magma types in the central Andes. Geological Society of America Bulletin 3, pp. 474-480. doi:10.1130/0016-7606(1976)87<474:ROPOTM>2.0.CO;2.

32. Fridriksson, T., Bjarni Reyr, K., Halldór, A., Eygerður, M., Snjólaug, Ó., Chiodini, G., 2006. CO_2 emissions and heat flow through soil, fumaroles, and steam heated mud pools at the Reykjanes geothermal area, SW Iceland. Applied Geochemistry, 21, 9, pp. 1551-1569. https://doi.org/10.1016/j.apgeochem.2006.04.006.

33. Fulignati, P., Gioncada, A., Sbrana, A., 1996. Modello geologico del sistema idrotermale-magmatico di Vulcano. In: La Volpe, L., Dellino, P., Nuccio, M., Privitera, E., Sbrana, A. (Eds.), Progetto Vulcano. Risultati delle Attività di Ricerca 1993-1995, pp. 97-118.

34. Giammanco, S., Melián, G., Neri, M., Hernández, P.A., Sortino, F., Barrancos, J., López, M., Pecoraino, G., Perez, N.M., 2016. Active tectonic features and structural dynamics of the summit area of Mt. Etna (Italy) revealed by soil CO_2 and soil temperature surveying. Journal of Volcanology and Geothermal Research, 311, pp. 79-98. https://doi.org/10.1016/j.jvolgeores.2016.01.004.

35. Giordano, G. Pinton, A., Cianfarra, P., Baez, W., Chiodi, A., Viramonte, J., Norini, G., Groppelli, G., 2013. Structural control on geothermal circulation in the Cerro Tuzgle–Tocomar geothermal volcanic area (Puna plateau, Argentina). Journal of Volcanology and Geothermal Research, 249, pp. 77-94. http://dx.doi.org/10.1016/j.jvolgeores.2012.09.009.

36. Godoy, B., Wörner, G., Kojima, S., Aguilera, F., Simon, K., Hartmann, G., 2014. Low-pressure evolution of arc magmas in thickened crust: the San Pedro-Linzor volcanic chain, Central Andes, Northern Chile. Journal of South American Earth Sciences 52, pp. 24-42. http://dx.doi.org/10.1016/j.jsames.2014.02.004.

37. Godoy, B., Taussi, M., González-Maurel, O., Renzulli, A., Hernández-Prat, L., le Roux, P., Morata, D., Menzies, A., 2019. Linking the mafic volcanism with the magmatic stages during the last 1 Ma in the main volcanic arc of the Altiplano-Puna Volcanic Complex (Central Andes). Journal of South American Earth Sciences, 95, 102295. https://doi.org/10.1016/j.jsames.2019.102295.

38. Gómez Diaz, E., Marín Cerón, M.I., 2020. Hydrogeochemical characteristics at Doña Juana Complex (SW Colombia): A new area for geothermal exploration in the Northern Andes region. Geothermics, 84, 101738. https://doi.org/10.1016/j.geothermics.2019.101738.

39. González-Ferran O, 1995. Volcanes de Chile. Santiago: Instituto Geográfico Militar chileno, 635 p.

40. Haffen, S., Diraison, M., Corsini, M., Géraud, Y., 2020. Geological model and fluid flow pathways of the Sol de Mañana/Apacheta geothermal field (Altiplano – Bolivia). Proceedings World Geothermal Congress 2020, Reykjavik, Iceland, May, 2021. https://pangea.stanford.edu/ERE/db/WGC/papers/WGC/2020/12136.pdf

41. Hanson, M.C., Oze, C., Horton, T.W., 2014. Identifying blind geothermal systems with soil CO_2 surveys. Applied Geochemistry, 50, pp. 106-114. http://dx.doi.org/10.1016/j.apgeochem.2014.08.009.

42. Harvey, M.C., Rowland, J.V., Chiodini, G., Rissmann, C., Bloomberg, S., Hernández, P.A., Mazot, A., Viveiros, F., Werner, C., 2015. Heat flux from magmatic hydrothermal systems related to availability of fluid recharge. Journal of Volcanology and Geothermal Research, 302, pp. 225-236. http://dx.doi.org/10.1016/j.jvolgeores.2015.07.003.

43. Harvey, M.C., Rowland, J.V., Chiodini, G., Rissmann, C.F., Bloomberg, S., Fridriksson, T., Oladottir, A.A., 2017. CO_2 flux geothermometer for geothermal exploration. Geochimica et Cosmochimica Acta, 213, pp. 1-16. http://dx.doi.org/10.1016/j.gca.2017.06.025.

44. Hauser, A., 1997. Register and characterization of mineral and thermal springs of Chile, 50. Servicio Nacional de Geología y Minería, Santiago, Chile, p. 90 (in Spanish).

45. Hernández, P.A., Pérez, N.M., Fridriksson, T., Jolie, E., Ilyinskaya, E., Thárhallsson, A., Ívarsson, G., Gíslason, G., Gunnarsson, I., Jónsson, B., Padrón, E., Melián, G., Mori, T, Notsu, K., 2012. Diffuse volcanic degassing and termal energy release from Hengill volcanic system, Iceland. Bulletin of Volcanology, 74, pp. 2435-2448. Doi: 10.1007/s00445-012-0673-2.

46. Hochstein, M.P., Bromley, C.J., 2005. Measurement of heat flux from steaming grounds. Geothermics, 34, pp. 133-160. doi:10.1016/j.geothermics.2004.04.002.

47. Hochstein, M.P., Browne, P.R.L., 2000. Surface manifestations of geothermal systems with volcanic heat sources. In: Encyclopedia of Volcanoes. A Press, pp. 835-855.

48. Hubbard, B.E., Crowley, J.K., 2005. Mineral mapping on the Chilean–Bolivian Altiplano using co-orbital ALI, ASTER and Hyperion imagery: Data dimensionality issues and solutions. Remote Sensing of Environment 99, pp. 173-186. doi:10.1016/j.rse.2005.04.027.

49. Hurwitz, S., Harris, R.N., Werner, C.A., Murphy, F., 2012. Heat flow in vapor dominated areas of the Yellowstone Plateau Volcanic Field: Implications for the thermal budget of the Yellowstone Caldera. Journal of Geophysical Research, vol. 117 (B10207). doi:10.1029/2012JB009463, 2012.

50. Jácome-Paz, M.P., Pérez-Zárate, D., Prol-Ledesma, R.M., Rodríguez-Díaz, A.A., Estrada-Murillo, A.M., González-Romo, I.A., Magaña-Torres, E., 2019. Two new geothermal prospects in the Mexican Volcanic Belt: La Escalera and Agua Caliente – Tzitzio geothermal springs, Michoacán, México. Geothermics, 80, pp. 44–55. https://doi.org/10.1016/j.geothermics.2019.02.004.

51. Jentsch, A., Jolie, E., Jones, D.G., Taylor-Curran, H., Peiffer, L., Zimmer, M., Lister, B., 2020. Magmatic volatiles to assess permeable volcano-tectonic structures in the Los Humeros geothermal field, Mexico. Journal of Volcanology and Geothermal Research, 394, 106820. https://doi.org/10.1016/j.jvolgeores.2020.106820.

52. Jolie, E., Klinkmueller, M., Moeck, I., 2015. Diffuse surface emanations as indicator of structural permeability in fault-controlled geothermal systems. Journal of Volcanology and Geothermal Research, 290, pp. 97-113. http://dx.doi.org/10.1016/j.jvolgeores.2014.11.003.

53. Krige, D.G., 1951. A statistical approach to some basic mine valuation problems on the Witwatersrand. Journal of the Southern African Institute of Mining and Metallurgy, 52, 119-139.

54. Lahsen, A., Rojas, J., Morata, D., Aravena, D., 2015. Geothermal exploration in Chile: Country Update. Proceedings of the World Geothermal Congress, Melbourne, Australia, 19 - 25 April 2015.

55. Lamberti, M.C., Vigide, N., Venturi, S., Agusto, M., Yagupsky, D., Winocur, D., Barcelona, H., Velez, M.L., Cardellini, C., Tassi, F., 2019. Structural architecture releasing deep-sourced carbon dioxide diffuse degassing at the Caviahue – Copahue Volcanic Complex. Journal of Volcanology and Geothermal Research, 374, pp. 131-141. https://doi.org/10.1016/j.jvolgeores.2019.02.004.

56. Lelli, M., Raco, B., 2017. A reliable and effective methodology to monitor CO_2 flux from soil: The case of Lipari Island (Sicily, Italy). Applied Geochemistry, 85, pp. 73-85. https://doi.org/10.1016/j.apgeochem.2017.08.004.

57. Lelli, M., 2018. Socompa Geothermal Prospect. Report on Water Geochemistry. Buenos Aires, Consiglio Nazionale delle Ricerche. Istituto di Geoscienze e Georisorse. Servicio Geológico Minero Argentino. 25 pp. http://repositorio.segemar.gov.ar/308849217/2430.

58. Lopez, T., Aguilera, F., Tassi, F., De Moor, J.M., Bobrowski, N., Aiuppa, A., Tamburello, G., Rizzo, A.L., Liuzzo, M., Viveiros, F., Cardellini, C., Silva, C., Fischer, T., Jean-Baptiste, P., Kazayaha, R., Hidalgo, S., Malowany, K., Lucic, G., Bagnato, E., Bergsson, B., Reath, K., Liotta, M., Carn, S., Chiodini, G., 2018. New insights into the magmatic-hydrothermal system and volatile budget of Lastarria volcano, Chile: integrated results from the 2014 IAVCEI CCVG 12th Volcanic Gas Workshop. Geosphere, 14 (3), pp. 1-25. doi:10.1130/GES01495.1.

59. Matheron, G., 1970. The theory of regionalized variables and its applications. Fascicule n. 5, Les Cahiers du Centre De Morphologie Mathématique, Ecole des Mines de Paris, Fontainebleau, pp. 211.

60. Maza, S.N., Collo, G., Morata, D., Lizana, C., Camus, E., Taussi, M., Renzulli, A., Mattioli, M., Godoy, B., Alvear, B., Pizarro, M., Ramírez, C., Rivera, G., 2018a. Clay mineral associations in the clay cap from the Cerro Pabellón blind geothermal system, Andean Cordillera, Northern Chile. Clay Minerals Journal of Fine Particle Science, 54 (2), 117–141. https://doi.org/10.1180/clm.2018.9.

61. Maza, S.N., Taussi, M., Camus, E., Collo, G., Morata, D., Renzulli, A., Mattioli, M., 2018b. Dynamics of a steam-heated alteration in the Apacheta volcano associated with the Cerro Pabellón blind geothermal system, Northern Chile. Libro de Actas, XV Congreso Geológico Chileno “Geociencias hacia la comunidad”, Concepción, 18–23 November, 2018, p. 407.

62. Maza, S.N., Taussi, M., Vidal, J., Collo, G., Renzulli, A., Morata, D., 2020. Studies of superficial hydrothermal alteration in the Inacaliri volcano: a new active geothermal system within the graben of the Cerro Pabellón blind geothermal system, northern Chile. Cities on Volcanoes 11, Heraklion, Crete, June 2021.

63. McMillan, N., Larson, P., Fairley, J., Mulvaney-Norris, J., Lindsey, C., 2018. Direct measurement of advective heat flux from several Yellowstone hot springs, Wyoming, USA. Geosphere 14 (4), pp. 1860-1874, https://doi.org/10.1130/GES01598.1.

64. Mesa de Geotermia, 2018. Rol de la geotermia en el desarrollo de la matriz eléctrica chilena. Ministerio de Energía, Chile. 66 pp. http://www.minenergia.cl/mesa-geotermia.

65. Morata, D., Aravena, D., Lahsen, A., Muñoz, M., Valdenegro, P., 2020a. Chile Up-Date: The First South American Geothermal Power Plant After One Century of Exploration. Proceedings World Geothermal Congress 2020, Reykjavik, Iceland, May 2021. https://pangea.stanford.edu/ERE/db/WGC/papers/WGC/2020/01064.pdf

66. Morata, D., Maza, S., Vidal, J., Taussi, M., Renzulli, A., Mattioli, M., Pizarro, M., Camus, E., Godoy, B., Alvear, B., Rivera, G., 2020b. Hydrothermal Alteration in Cerro Pabellón Geothermal Field: from Surface and Drill Core Data to Conceptual Model. Proceedings World Geothermal Congress 2020, Reykjavik, Iceland, May 2021. https://pangea.stanford.edu/ERE/db/WGC/papers/WGC/2020/12048.pdf

67. Navarrete-Calvo, A.A., 2012. Origen y comportamiento del CO_2 difuso del suelo en los sistemas geotérmicos de Juncalito (68°55'50-68°38'20''W y 26°25'- 26°31'30''S, Región de Atacama) y Colpitas (69°29'30''-69°23'30''W y 17°50'30''S-18°S, Región de Arica y Parinacota), Chile. Dissertation, Bachelor's Degree Thesis (in Spanish), Universidad de Chile. Chile, Santiago.

68. Olmsted, F.H., Ingebritsen, S.E., 1986. Shallow subsurface temperature surveys in the Basin and Range Province - II. Ground temperatures in the Upsal Hogback geothermal area, West-Central Nevada, U.S.A. Geothermics, vol.15, pp. 267-275. https://doi.org/10.1016/0375-6505(86)90104-5.

69. Ostapenko, S.V., Spektor, S.V., Netesov, Y.P., 1998. San Jacinto–Tizate geothermal field, Nicaragua: exploration and conceptual model. Geothermics, 27, pp. 361-378. https://doi.org/10.1016/S0375-6505(98)00007-8.

70. Padrón, E., Hernández, P.A., Toulkeridis, T., Pérez, N.M., Marrero, R., Melián, G., Virgili, G., Notsu, K., 2008. Diffuse CO_2 emission rate from Pululahua and the lake-filled Cuicocha calderas, Ecuador. Journal of Volcanology and Geothermal Research, 176, pp. 163-169. doi:10.1016/j.jvolgeores.2007.11.023.

71. Piscaglia, F., 2011. The high temperature geothermal field of the Apacheta-Aguilucho Volcanic Complex (northern Chile): geo-petrographic surface exploration, crustal heat sources and cap rocks. PhD Thesis (in Italian), University of Urbino, Italy, pp. 188.

72. Price, A.N., Lindsey, C.R., Fairley, J.P., 2017. Interpretation of Ground Temperature Anomalies in Hydrothermal Discharge Areas. Water Resources Research, 53. https://doi.org/10.1002/2017WR021077.

73. Procesi, M., 2014. Geothermal potential evaluation for northern Chile and suggestions for new energy plans. Energies 7, pp. 5444-5459. doi:10.3390/en7085444.

74. Raco, B., 2018. Socompa Geothermal Prospect. Report on Fluid Geochemistry (Soil CO_2 degassing). Buenos Aires, Consiglio Nazionale delle Ricerche. Istituto di Geoscienze e Georisorse. Servicio Geológico Minero Argentino. 20 pp. http://repositorio.segemar.gov.ar/308849217/2429

75. Raich, J.W., Schlesinger, W.H., 1992. The global carbon dioxide flux in soil respiration and its relationship to vegetation and climate. Tellus, 44B, pp. 81-99. https://doi.org/10.1034/j.1600-0889.1992.t01-1-00001.x.

76. Renzulli, A., Menna, M., Tibaldi, A., Flude, S., 2006. New data of surface geology, petrology and Ar-Ar geochronology of the Altiplano-Puna Volcanic Complex (northern Chile) in the framework of future geothermal exploration. XI Congreso Geòlogico Chileno, Antofagasta, 7-11 August.

77. Risacher, F., Fritz, B., Hauser, A., 2011. Origin of components in Chilean thermal waters. Journal of South American Earth Sciences, 31, pp. 153-170. doi:10.1016/j.jsames.2010.07.002

78. Rissmann, C., Christenson, B., Werner, C., Leybourne, M., Cole, J., Gravley, D., 2012. Surface heat flow and CO_2 emissions within the Ohaaki hydrothermal field, Taupo Volcanic Zone, New Zealand. Applied Geochemistry, 27, pp. 223-239. doi:10.1016/j.apgeochem.2011.10.006.

79. Rivera, G., Morata, D., Ramírez, C., 2015. Evolución vulcanologíca y tectónica del área del Cordón Volcánico Cerro del Azufre – Cerro Inacaliri y su relación con el sistema geotérmico de Pampa Apacheta, II Región de Antofagasta, Chile. In Actas XIV Congreso Geológico Chileno, La Serena, Chile, pp. 556-559.

80. Rogers, G.F.C., Mayhew, Y.R., 1995. Thermodynamic and Transport Properties of Fluids. Blackwell Publishing Ltd., Oxford (UK).

81. Rolleau, E., Bravo, F., Pinti, D.L., Barde-Cabusson, S., Pizarro, M., Tardani, D., Muñoz, C., Sanchez, J., Sano, Y., Takahata, N., de la Cal, F., Esteban, C., Morata, D., 2017. Structural controls on fluid circulation at the Caviahue-Copahue Volcanic Complex (CCVC) geothermal area (Chile-Argentina), revealed by soil CO_2 and temperature, self-potential, and helium isotopes. Journal of Volcanology and Geothermal Research, 341, pp. 104-118. http://dx.doi.org/10.1016/j.jvolgeores.2017.05.010.

82. Salisbury, M.J., Jicha, B.R., de Silva, S.L., Singer, B.S., Jiménez, N.C., Ort, M.H., 2011. $^{40}Ar/^{39}Ar$ chronostratigraphy of Altiplano-Puna volcanic complex ignimbrites reveals the development of a major magmatic province. Geological Society of America Bulletin 123, pp. 821-840. https://doi.org/10.1130/B30280.1.

83. Sanchez-Alfaro, P., Sielfeld, G., Van Campen, B., Dobson, P., Fuentes, V., Reed, A., Palma-Behnke, R., Morata, D., 2015. Geothermal barriers, policies and economics in Chile – Lessons for the Andes. Renewable and Sustainable Energy Reviews, 51, pp. 1390-1401. http://dx.doi.org/10.1016/j.rser.2015.07.001.

84. Sbrana, A., Marianelli, P., Belgiorno, M., Sbrana, M., Ciani, V., 2020. Natural CO_2 degassing in the Mount Amiata volcanic–geothermal area. Journal of Volcanology and Geothermal Research, 397, 106852. https://doi.org/10.1016/j.jvolgeores.2020.106852.

85. Sellés, D., Gardeweg, M., 2017. Geología del área Ascotán-Cerro Inacaliri, Región de Antofagasta. Servicio Nacional de Geología y Minería, Carta Geológica de Chile, Serie Geología Básica No. 190, pp. 73, 1 mapa escala 1:100.000, 1 CD con anexos. Santiago (Chile). doi:10.13140/RG.2.2.30946.84165.

86. Sinclair, A.J., 1974. Selection of threshold values in geochemical data using probability graphs. Journal of Geochemical Exploration, 3, pp. 129-149. https://doi.org/10.1016/0375-6742(74)90030-2.

87. Sorey, M.L., Colvard, E.M., 1994. Measurements of heat and mass flow from thermal areas in Lassen Volcanic National Park, California, 1984-93. Water-Resources Investigations Report 94-4180-A. https://doi.org/10.3133/wri944180A.

88. Tamburello, G., Pondrelli, S., Chiodini, G., Rouwet, D., 2018. Global-scale control of extensional tectonics on CO_2 earth degassing. Nature Communications, 9:4608. doi: 10.1038/s41467-018-07087-z.

89. Tassi, F., Aguilera, F., Darrah, T., Vaselli, O., Capaccioni, B., Poreda, R.J., Delgado Huertas, A., 2010. Fluid geochemistry of hydrothermal systems in the Arica-Parinacota, Tarapacá and Antofagasta regions (northern Chile). Journal of Volcanology and Geothermal Research, 192, pp. 1-15. doi:10.1016/j.jvolgeores.2010.02.006.

90. Taussi, M., Nisi, B., Pizarro, M., Morata, D., Veloso, E.A., Volpi, G., Vaselli, O., Renzulli, A., 2019a. Sealing capacity of clay-cap units above the Cerro Pabellón hidden geothermal system (northern Chile) derived by soil CO_2 flux and temperature measurements. Journal of Volcanology and Geothermal Research, 384, pp. 1-14. https://doi.org/10.1016/j.jvolgeores.2019.07.009.

91. Taussi, M., Godoy, B., Piscaglia, F., Morata, D., Agostini, S., Le Roux, P., Gonzalez-Maurel, O., Gallmeyer, G., Menzies, A., Renzulli, A., 2019b. The upper crustal magma plumbing system of the Pleistocene Apacheta-Aguilucho Volcanic Complex area (Altiplano-Puna, northern Chile) as inferred from the erupted lavas and their enclaves. Journal of Volcanology and Geothermal Research, 373, pp. 179-198. https://doi.org/10.1016/j.jvolgeores.2019.01.021.

92. Tibaldi, A., 1995. Morphology of pyroclastic cones and tectonics. Journal of Geophysical Research, vol. 100, B12, pp. 24521-24535. https://doi.org/10.1029/95JB02250.

93. Tibaldi, A., Corazzato, C., Rovida, A., 2009. Miocene-Quaternary structural evolution of the Uyuni-Atacama region, Andes of Chile and Bolivia. Tectonophysics 471 (1-2), pp. 114-135. doi:10.1016/j.tecto.2008.09.011.

94. Tibaldi, A., Rust, D., Corazzato, C., Merri, A., 2010. Setting the scene for self-destruction: From sheet intrusions to the structural evolution of rifted stratovolcanoes. Geosphere, 6, pp. 189-210. doi: 10.1130/GES00521.1.

95. Tibaldi, A., Bonali, F.L., Corazzato, C., 2017. Structural control on volcanoes and magma paths from local- to orogen-scale: The central Andes case. Tectonophysics, 699, pp. 16-41. http://dx.doi.org/10.1016/j.tecto.2017.01.005.

96. Tibaldi, A., Bonali, F.L., 2018. Contemporary recent extension and compression in the central Andes. Journal of Structural Geology 107, pp. 73-92. doi:10.1016/j.jsg.2017.12.004.

97. Urzua, L., Powell, T., Cumming, W.B., Dobson, P., 2002. Apacheta, a new geothermal prospect in northern Chile. Geothermal Resources Council 26, pp. 65-69.

98. Veloso, E.A., Tardani, D., Elizalde, D., Godoy, B.E., Sanchez-Alfaro, P., Aron, F., Reich, M., Morata, D., 2019. A review of the geodynamic constraints on the development and evolution of geothermal systems in the Central Andean Volcanic Zone (18–28°Lat.S). International Geology Review, pp. 1-25. https://doi.org/10.1080/00206814.2019.1644678.

99. Venturi, S., Tassi, F., Bicocchi, G., Cabassi, J., Capecchiacci, F., Capasso, G., Vaselli, O., Ricci, A., Grassa, F., 2017. Fractionation processes affecting the stable carbon isotope signature of thermal waters from hydrothermal/volcanic systems: The examples of Campi Flegrei and Vulcano Island (southern Italy). Journal of Volcanology and Geothermal Research, 345, pp. 46-57. http://dx.doi.org/10.1016/j.jvolgeores.2017.08.001.

100. Venturi, S., Tassi, F., Magi, F., Cabassi, J., Ricci, A., Capecchiacci, F., Caponi, C., Nisi, B., Vaselli, O., 2019. Carbon isotopic signature of interstitial soil gases reveals the potential role of ecosystems in mitigating geogenic greenhouse gas emissions: Case studies from hydrothermal systems in Italy. Science of the Total Environment, 655, pp. 887-898. https://doi.org/10.1016/j.scitotenv.2018.11.293.

101. Villaroel, D.G., 2020. Geothermal Development in Bolivia - A Country Update. Proceedings World Geothermal Congress 2020, Reykjavik, Iceland, May 2021. https://pangea.stanford.edu/ERE/db/WGC/papers/WGC/2020/01034.pdf

102. Viveiros, F., Cardellini, C., Ferreira, T., Caliro, S., Chiodini, G., Silva, C., 2010. Soil CO_2 emissions at Furnas volcano, São Miguel Island, Azores archipelago: Volcano monitoring perspectives, geomorphologic studies, and land use planning application. Journal of Geophysical Research, 115, B12208. doi:10.1029/2010JB007555.

103. Ward, K.M., Zandt, G., Beck, S.L., Christensen, D.H., McFarlin, H., 2014. Seismic imaging of the magmatic underpinnings beneath the Altiplano-Puna volcanic complex from the joint inversion of surface wave dispersion and receiver functions. Earth and Planetary Science Letters 404, pp. 43-53. https://doi.org/10.1016/j.epsl.2014.07.022.

104. Werner, C.A., Hochstein, M.P., Bromley, C.J., 2004. CO_2-flux of steaming ground at Karapiti, Wairakei. Proceedings of the 26th New Zealand Geothermal Workshop 2004, pp. 59-64.

105. Werner, C., Cardellini, C., 2006. Comparison of carbon dioxide emissions with fluid upflow, chemistry, and geologic structures at the Rotorua geothermal system, New Zealand. Geothermics, 35, pp. 221-238. doi:10.1016/j.geothermics.2006.02.006.

106. Zarrouk, S.J., Moon, H, 2014. Efficiency of geothermal power plants: A worldwide review. Geothermics, vol. 51, pp. 142-153. https://doi.org/10.1016/j.geothermics.2013.11.001.